CrossMark

ORIGINAL PAPER

Trace element mapping by LA-ICP-MS: assessing geochemical mobility in garnet

Tom Raimondo[1] · Justin Payne[1] · Benjamin Wade[2] · Pierre Lanari[3] · Chris Clark[4] · Martin Hand[5]

Abstract A persistent problem in the study of garnet geochemistry is that the consideration of major elements alone excludes a wealth of information preserved by trace elements, particularly the rare-earth elements (REEs). This is despite the fact that trace elements are generally less vulnerable to diffusive resetting, and are sensitive to a broader spectrum of geochemical interactions involving the entire mineral assemblage, including the growth and/or dissolution of accessory minerals. We outline a technique for the routine acquisition of high-resolution 2D trace element maps by LA-ICP-MS, and introduce an extension of the software package *XMapTools* for rapid processing of LA-ICP-MS data to visualise and interpret compositional zoning patterns. These methods form the basis for investigating the mechanisms controlling geochemical mobility in garnet, which are argued to be largely dependent on the interplay between element fractionation, mineral reactions and partitioning, and the length scales of intergranular transport. Samples from the Peaked Hill shear zone, Reynolds Range, central Australia, exhibit contrasting trace element distributions that can be linked to a detailed sequence of growth and dissolution events. Trace element mapping is thus employed to place garnet evolution in a specific paragenetic context and derive absolute age information by integration with existing U–Pb monazite and Sm–Nd garnet geochronology. Ultimately, the remarkable preservation of original growth zoning and its subtle modification by subsequent re-equilibration is used to 'see through' multiple superimposed events, thereby revealing a previously obscure petrological and temporal record of metamorphism, metasomatism, and deformation.

Keywords Garnet zoning · Trace element · Rare-earth element · LA-ICP-MS · Diffusion · Metasomatism

✉ Tom Raimondo
tom.raimondo@unisa.edu.au

1 School of Natural and Built Environments, University of South Australia, GPO Box 2471, Adelaide, SA 5001, Australia

2 Adelaide Microscopy, University of Adelaide, Adelaide, SA 5005, Australia

3 Institute of Geological Sciences, University of Bern, Baltzestrasse 1+3, 3012 Bern, Switzerland

4 Department of Applied Geology, Curtin University, GPO Box U1987, Perth, WA 6845, Australia

5 School of Physical Sciences, University of Adelaide, Adelaide, SA 5005, Australia

Introduction

Garnet holds a unique place in metamorphic petrology as a singularly useful mineral to reconstruct the pressure–temperature–time (P–T–t) evolution of Earth's crust. This is largely due to its ubiquity in medium- and high-grade metamorphic rocks, its occurrence in mineral assemblages of interest for thermobarometry, its utility as a geochronometer, and most importantly its ability to preserve chemical zoning representing the history of dynamic changes experienced by a rock mass (e.g., Kohn 2003; Ague and Carlson 2013; Baxter and Scherer 2013; Caddick and Kohn 2013 and references therein). Where rock-wide chemical equilibration is achieved, garnet growth zoning reflects

🖄 Springer

progressive crystallisation coeval with changes in *P–T* conditions or bulk rock chemistry. It is therefore particularly useful to unravel the thermobarometric evolution of open systems, the development of mineral parageneses, and the crystallisation mechanisms involved (e.g., Hollister 1966; Cygan and Lasaga 1982; Loomis and Nimick 1982; Spear and Selverstone 1983; Konrad-Schmolke et al. 2005). In the case of kinetically-controlled crystallisation, it can also reveal detailed information about the rates and length scales of partial chemical equilibration (e.g., Spear and Daniel 2001; Yang and Rivers 2001; Skora et al. 2006; Carlson 2011).

However, growth zoning in major elements is commonly altered by volume diffusion, which is particularly efficient at high temperatures for elements with high diffusion coefficients, such as Fe and Mg (e.g., Chakraborty and Ganguly 1992; Carlson 2002, 2006; Ganguly 2010). In such cases, geochemical information relating to the conditions and mechanisms of garnet growth (particularly its prograde evolution) is either totally or partially obliterated (e.g., Florence and Spear 1991; Kohn 2003; Caddick et al. 2010; Ague and Axler 2016). To maximise the amount of information retained despite this modification process, trace elements (particularly REEs) can be a more robust geochemical archive because of their lower diffusion coefficients compared to major elements. They can also provide insight into parts of the mineral reaction history that exclude the major elements, such as the growth and dissolution of accessory minerals, including zircon and monazite (Lanzirotti 1995; Pyle and Spear 2003; Kelsey and Powell 2011; Carlson 2012; Moore et al. 2013).

Common instrumentation used to interrogate trace element distributions in geological samples includes electron probe microanalysis (EPMA), transmission electron microscopy (TEM), scanning electron microscopy (SEM), secondary ion mass spectrometry (SIMS), and synchrotron X-ray fluorescence or diffraction analysis (XRF/XRD). Each technique has its inherent strengths and limitations, whether they relate to detection limits, analytical volumes, sample preparation, and/or instrument cost and accessibility. Traditionally, laser ablation–inductively coupled plasma–mass spectrometry (LA-ICP-MS) has been used to quantify major and trace element (wt%–ppb) content in a wide variety of geological materials via spot analysis (Jackson et al. 1992; Norman et al. 1996; Günther et al. 1997; Heinrich et al. 2003). However, its utility as an imaging tool has recently emerged to allow 2D mapping with excellent detection limits (ppb) over a wide isotopic range (^{7}Li to ^{238}U), with minimal sample preparation required. This is achieved by rastering of the focused laser beam in linear transects, which are then stitched together by post-acquisition processing to form a quantified image of the trace element distribution (Woodhead et al. 2007; Ulrich

et al. 2009; Rittner and Müller 2012; Paul et al. 2012, 2014; Ubide et al. 2015). Large suites of isotopes can be collected concurrently, including multiple isotopes of the same element (detection limits and instrument interferences permitting), providing access to substantially increased geochemical information from analysed samples.

In this contribution, we demonstrate use of the LA-ICP-MS imaging technique to reveal complex trace element zoning patterns in garnet affected by fluid–rock interaction in a mid-crustal shear zone. Garnet–staurolite–kyanite–biotite–muscovite schists from Peaked Hill, Reynolds Range, central Australia, are characterised by two distinctive garnet varieties with contrasting textural and compositional characteristics. High-resolution trace element maps are combined with existing EPMA major element and SIMS oxygen isotope data sets, along with U–Pb monazite and Sm–Nd garnet geochronology, to investigate the record of geochemical mobility during a prolonged sequence of high-grade metamorphism, deformation, and metasomatism. A principal focus of this study is the length- and time scales across which intragrain zoning is preserved, and the progressive development of mineral assemblages in response to these superimposed events.

Outcrop relationships and sample descriptions

Peaked Hill is located at the south-eastern margin of the Reynolds Range, central Australia, approximately 18 km north of the township of Aileron (Fig. 1). It consists of a series of low hills mostly composed of megacrystic granitic gneiss (Boothby Orthogneiss), with small exposures of pelitic granulite (Aileron Metamorphics). The outcrops are dissected by an array of steeply-dipping NW/SE-trending shear zones up to 20 m in width, many of which form prominent bladed rocks that wrap around the base of each hill. A thin (1–2 m wide) shear zone dissecting the dominant granitic wall rocks is discussed by Cartwright and Buick (1999). A parallel structure approximately 2 km north of this location transects one of the minor metapelitic lenses, and is described in detail by Raimondo et al. (2012).

The granulite wall rocks comprise a thinly interlayered pelitic/psammitic gneiss containing garnet–sillimanite–cordierite–K-feldspar–biotite–quartz assemblages, similar to that described by Morrissey et al. (2014) and Howlett et al. (2015) from adjacent parts of the Reynolds Range. In a steeply-dipping shear zone, approximately 10 m in width, the gneissic precursor is altered to a garnet–staurolite–kyanite–biotite–muscovite schist. Broad, open folds and irregular compositional layering that characterise the gneiss are truncated by the schistose shear fabric, with a sharp strain gradient matching the boundary of strong mineralogical alteration. Peak *P–T* conditions associated with shearing are estimated at 500–600 °C and
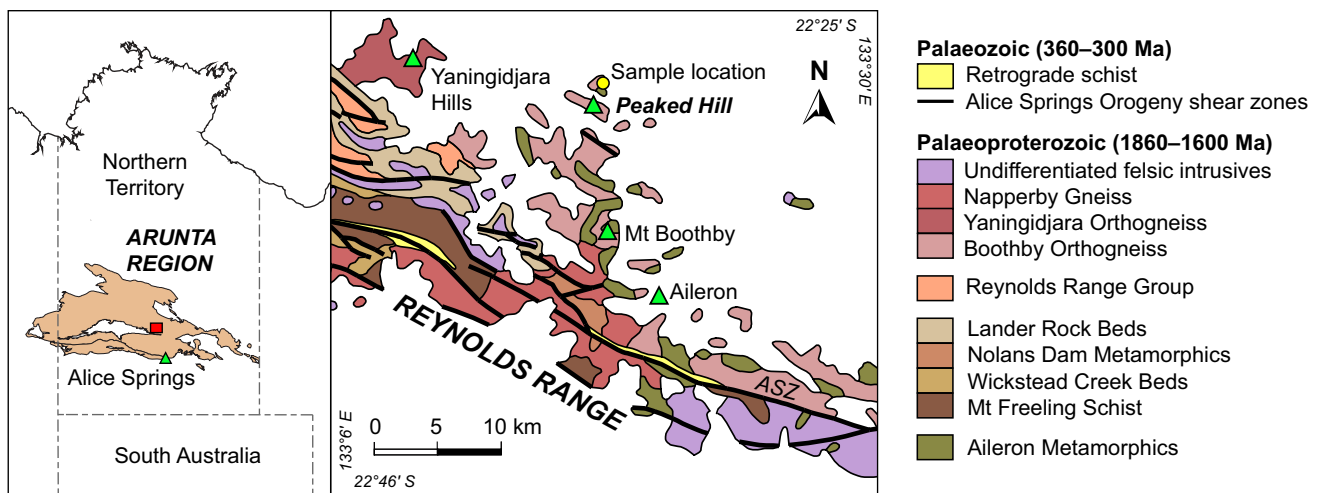
Fig. 1 Generalised geology of the Reynolds Range, central Australia, showing the distribution of major rock types and shear zones. The location of all samples presented in this study is indicated by a *yellow circle* immediately north of the Peaked Hill locality. Map area corresponds to the *red box* indicated on the *inset* panel of the Arunta Region. *ASZ* Aileron Shear Zone. Figure modified from Raimondo et al. (2012)

5.0–6.5 kbar in this area, following a trend of increasing metamorphic grade towards the south-eastern margin of the Reynolds Range (Dirks and Wilson 1990; Dirks et al. 1991; Cartwright and Buick 1999; Hand and Buick 2001; Raimondo et al. 2011).

Two garnet-bearing samples from the existing study of Raimondo et al. (2012) were selected for further characterisation by LA-ICP-MS to investigate the trace element record of fluid–rock interaction: PH2-E and PH4, located within 5 m of each other from the same shear zone outcrop. These samples were chosen on the basis that they exhibit contrasting textural and compositional features that reflect different paragenetic histories and geochemical changes indicative of complex grain-scale interactions during metasomatism. Such features include substantial differences in garnet size, morphology, and microstructure, along with variable records of major element and oxygen isotope exchange measured by EPMA and SIMS diffusion profiles.

Petrographic descriptions of both shear zone samples and their immediate wall rocks are provided in Raimondo et al. (2012), and only essential details are repeated here. Sample PH2-E contains coarse (1–5 mm) staurolite poikiloblasts and smaller (0.5–2 mm) euhedral garnet porphyroblasts associated with thick seams of aligned biotite and muscovite, recrystallised quartz ribbons and minor plagioclase (Fig. 2a, b). Garnet is largely inclusion-free except for minor quartz, biotite and ilmenite, and shows little evidence of fracturing or corroded grain boundaries. Linear trails of monazite included in matrix biotite (Fig. 2b) record a U–Pb age of 354 ± 3 Ma (Raimondo et al. 2012), consistent with deformation and metasomatism during the Ordovician–Carboniferous (450–300 Ma) Alice Springs Orogeny (Haines et al. 2001; Buick et al. 2008; McLaren et al. 2009; Raimondo et al. 2014). An Sm–Nd isochron age of 333 ± 20 Ma has also been obtained from this sample by Raimondo et al. (2012), although these authors raised a concern regarding its analytical precision that this study addresses in more detail.

Sample PH4 features elongate aggregates of large (0.3–1.5 cm) garnet porphyroclasts (Fig. 2c, d) that form 'stringy' grain shapes reminiscent of its gneissic precursor (Fig. 2e). The garnet aggregates are dissected by multiple fractures that create a closely-spaced mosaic pattern, and are segregated into thick seams enclosed by muscovite and biotite foliae that define the schistose shear fabric. Fibrous sillimanite inclusion trails are continuous across adjacent garnet fragments (Fig. 2d), and again match similar features in garnet from the wall rock (Fig. 2e). Staurolite and kyanite occur as coarse (0.5–3 mm) porphyroblasts associated with biotite, whereas quartz occurs in the matrix as fine recrystallised ribbons. Similar to PH2-E, monazite grains are arranged in distinctive linear arrays in matrix biotite, and record a U–Pb age of 360 ± 3 Ma (Raimondo et al. 2012).

Methods

Data acquisition

LA-ICP-MS trace element maps were acquired using a Resonetics M-50-LR 193 nm excimer laser coupled to an Agilent 7700x Quadrupole ICP-MS housed at Adelaide Microscopy, University of Adelaide. Instrument
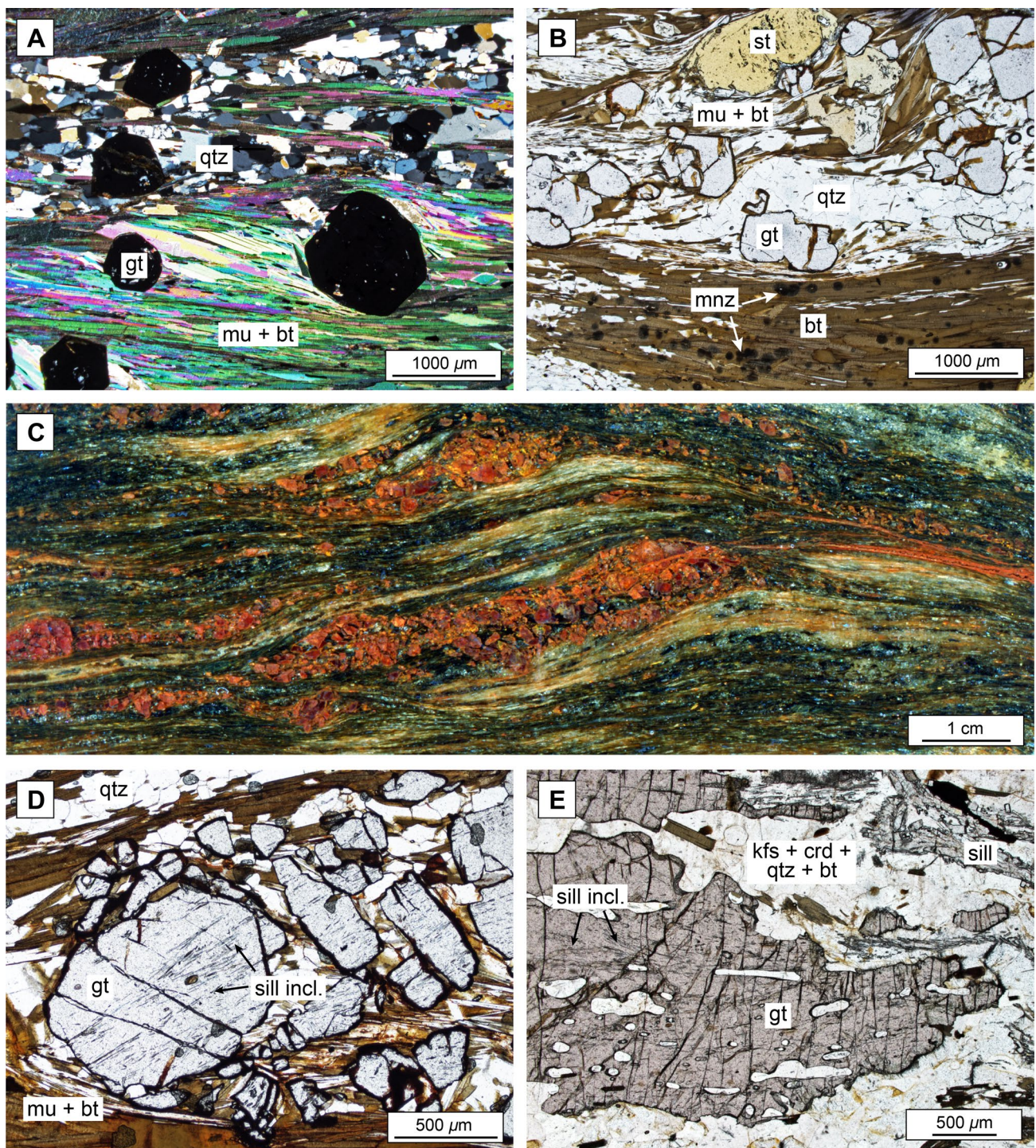
Fig. 2 Transmitted light photomicrographs and a rock block scan of key mineral textures from the Peaked Hill samples. **a** Euhedral garnet porphyroblasts from sample PH2-E, wrapped by quartz ribbons and seams of intergrown biotite and muscovite. **b** Staurolite and garnet porphyroblasts and linear inclusion trails of monazite from sample PH2-E. **c, d** Elongate aggregates of fractured garnet fragments from sample PH4, forming an interlinked mosaic texture enclosed by muscovite and biotite foliae defining the schistose shear fabric. In **d**, note the fine sillimanite inclusions that continue across several garnet fragments and match similar features in elongate garnet grains from the adjacent wall rock (PH09-1) shown in **e**. The wall rock comprises an interlayered pelitic/psammitic granulite characterised by garnet–cordierite–sillimanite–K-feldspar–biotite–quartz assemblages. Image **a** is in cross-polarized light; images **b–e** are in plane-polarized light. *Bt* biotite, *crd* cordierite, *gt* garnet, *incl.* inclusion, *kfs* K-feldspar, *mnz* monazite, *mu* muscovite, *sill* sillimanite, *st* staurolite, *qtz* quartz

conditions and mapping protocols similar to that employed in this study are outlined in several previous contributions from our laboratory, mostly pertaining to sulfides (e.g., Cook et al. 2013; Ingham et al. 2014; Lockington et al. 2014; George et al. 2015) and various silicates (e.g., Ismail et al. 2014; Kontonikas-Charos et al. 2014; Sharrad et al. 2014; Xu et al. 2016). Similar laser ablation imaging by other laboratories has also been performed on silicates by Ulrich et al. (2009), Paul et al. (2014), Ubide et al. (2015) and Petrelli et al. (2016). Details specific to the trace element analysis of garnet are provided in the following.

The Resonetics M-50 uses a two-volume laser ablation cell designed by Laurin Technic Pty that facilitates fast washout of ablated material (five orders of magnitude in 3 s, with no signal smoothing device used). Mapping was performed on standard 30 μm-thick polished thin sections mounted in a spring-loaded holder designed for 25 mm glass slides. Imaging was achieved by ablating a series of parallel rasters across the sample surface to form a square or rectangular grid (Fig. 3). Pre-ablation of each raster was completed to minimise the effect of redeposition, and 30 s of background measurement was also acquired prior to each scan. Ablation was performed in an atmosphere of UHP He (0.70 L min^{-1}), mixed with Ar (0.93 L min^{-1}) immediately after the ablation cell. A beam diameter of 16 μm coupled with a laser repetition rate of 10 Hz produced an energy density of ~7 J cm^{-2} at the target, and a scan speed of 22 μm s^{-1} and line spacing of 16 μm were employed. High fluence ensured that count rates were sufficient at the small spot sizes required for optimal spatial resolution, and trench depths were maintained at <5 μm given the scan speeds involved (Fig. 3).

Data acquisition was performed in time-resolved analysis mode as a single continuous experiment. Each analysis comprised a suite of 33 elements (Online Resources 1 and 2); dwell times for major elements were 0.005 s (to reduce excessive count rates) and all other masses were 0.008 s, giving a total sweep time of 0.31 s. Standards were analysed in duplicate at the start and end of each mapping run, and included reference glasses NIST 610 and 612 (Pearce et al. 1997; Jochum et al. 2011) and garnet standard MON-GT (Harris et al. 2000; Harris and Vogeli 2010). The total analysis time was approximately 4.5 h for an area of 1.4×1.4 mm on sample PH2-E and 21.5 h for an area of 3.8×5.4 mm on sample PH4, roughly comparable to the duration of typical EPMA X-ray maps of equivalent size.

Data reduction and quantification

Post-acquisition processing was performed using the software *Iolite* (Woodhead et al. 2007; Hellstrom et al. 2008; Paton et al. 2011), an open source add-in for *Igor Pro* (WaveMetrics) developed by the Melbourne Isotope Research Group at the University of Melbourne. Data reduction procedures followed those outlined by Ubide et al. (2015). Instrument drift and mass bias were corrected by applying a linear fit between sets of standards analysed at the start and end of each mapping run, and the average background was also subtracted from each raster. Background count rates for REEs are typically zero, requiring the calculation of detection limits following the
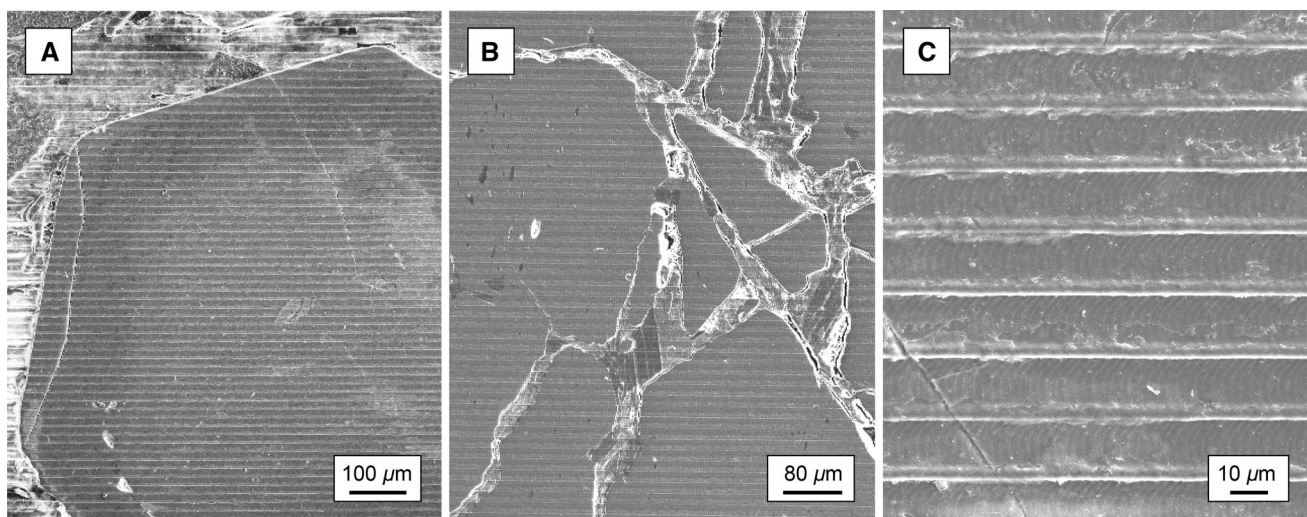

Fig. 3 Secondary electron (SE) images of garnet from **a** sample PH2-E and **b, c** sample PH4 taken subsequent to analysis, showing laser ablation rasters that were stitched together to form the composite trace element maps in Figs. 4, 5, 8, and 9. Note the thin white ridges caused by redeposition adjacent to ablation trenches; these features are <1 μm wide in each case, and the trench depth is <5 μm. The direction of laser scanning is from *left* to *right* in all images, and individual laser pulses are visible as *curved* trails in **c**

Limit of Quantification (LOQ) procedure of Howell et al. (2013). LOQ values are used as the minimum detection limit when extracting data from maps, either to create line profiles or apply the various image processing functions outlined in the following.

Quantification was performed using ^{29}Si for internal calibration based on a weighted average of EPMA wt% SiO_2 values across each garnet grain, and all rasters were stitched into a two-dimensional numerical array (matrix) containing the background- and drift-corrected ppm values for each element. Note that all maps have been quantified using SiO_2 calibration data for garnet alone. Hence, map areas corresponding to all other minerals present are indicative of relative changes in abundance only, as indicated by comparison with raw counts per second maps, and true compositional information will vary according to the degree of mismatch in SiO_2 content.

Image and data processing – *XMapTools*

Iolite saves the stitched images as individual files ('Waves') with quantified ppm data for each element presented as a numerical matrix that can be exported as delimited text. These data were imported into the *MAT-LAB*-based graphical user interface *XMapTools* 2.3.1 (Lanari et al. 2014), freely available online at http://www.xmaptools.com. This software enables simple application of a range of image and data processing tools such as contrast enhancement, colourmap editing, line profile creation, local bulk composition calculations, binary and ternary compositional plots, and phase identification/masking (e.g., Lanari et al. 2013, 2014; Mészáros et al. 2016). We have also incorporated several new functions specific to the processing and manipulation of LA-ICP-MS data that are available in the latest release. These include modules for multi-element RGB image stacks, trace element ratio calculations, and normalised REE diagrams ('spider plots'). Figures 5 and 9 contain composite RGB images constructed by assigning the Ce, Gd, and Lu maps to the red, green, and blue channels, respectively. Any alternative combination of the available trace element maps is also possible. Figures 6 and 10 illustrate use of the line mode sampling function to generate quantified compositional profiles in any orientation. Figure 11 demonstrates use of the *Chem2D* module to create binary scatter plots and corresponding pixel identification maps of garnet REE concentrations. Finally, Fig. 12 shows normalised REE diagrams constructed from map data using the *Spider* module. The reader is referred to Lanari et al. (2014) and the *XMapTools* user guide (available online at http://www.xmaptools.com) for a more detailed description of these functions and their application.

Results

From the suite of 33 elements collected for each mapping run, a subset of the most indicative elements and multi-element RGB stacks are shown in Figs. 4 and 5 for PH2-E and Figs. 8 and 9 for PH4, with existing major element EPMA X-ray maps from Raimondo et al. (2012) provided for comparison. The remaining elements not shown are available in Online Resource 1 (PH2-E) and Online Resource 2 (PH4). Line profiles extracted from the image data are shown in Figs. 6, 7, and 10.

Sample PH2-E

LA-ICP-MS major element maps from PH2-E (Fig. 4) show good correspondence to EPMA X-ray maps from the same sample, with Fe, Mg, and Mn displaying smooth radial zoning. Ca shows a progressively decreasing trend that is slightly patchy and irregular, a feature more apparent on the EPMA map. A thin zone of Mn enrichment at the garnet rim is matched by sharp decreases in Fe and Mg. Ilmenite inclusions appear as bright spots on the Fe maps, whereas quartz inclusions appear as dark spots on all major element maps, features that are again better resolved on the EPMA maps.

The smooth zoning patterns for Fe, Mg, and Mn are noticeably decoupled from that of most trace elements (Fig. 5). Cr displays a convoluted distribution that is somewhat analogous to the EPMA Ca map, with a 'spiral' structure of successive peaks and troughs from core to rim. Heavy rare-earth elements (HREEs) show an irregularly-shaped core domain that is succeeded by roughly concentric decreasing trends from core to rim, punctuated by a series of successive peaks and sharp depletions that mark successive annuli. Zr shows a similar decreasing trend, whereas Ti is largely flat except for isolated inclusions. Along line A–B (Fig. 6), note that the HREE-enriched inner core has the steepest gradient for the heaviest masses such as Lu and Yb, becoming increasingly shallow for lighter masses such as Dy and Ho, although superimposed peaks occur in the same radial position for all elements along the entire length of the profile (Fig. 7). All HREEs and Zr also feature two distinctive satellite peaks at the outermost rim that are separated by a thin trough; this pattern encircles the entire grain boundary, except where the inner satellite peak is truncated at an embayed section directly adjacent to matrix biotite (white arrows on Er and Ho maps in Fig. 5).

Light rare-earth element (LREE) zoning is difficult to detect in the core domain, where most ppm values approach or are at detection limits, but appears as an increasing trend towards the rim for more abundant medium rare-earth elements (MREEs) such as Sm, Gd, and Tb. There are occasional bright spots that correspond to monazite and zircon
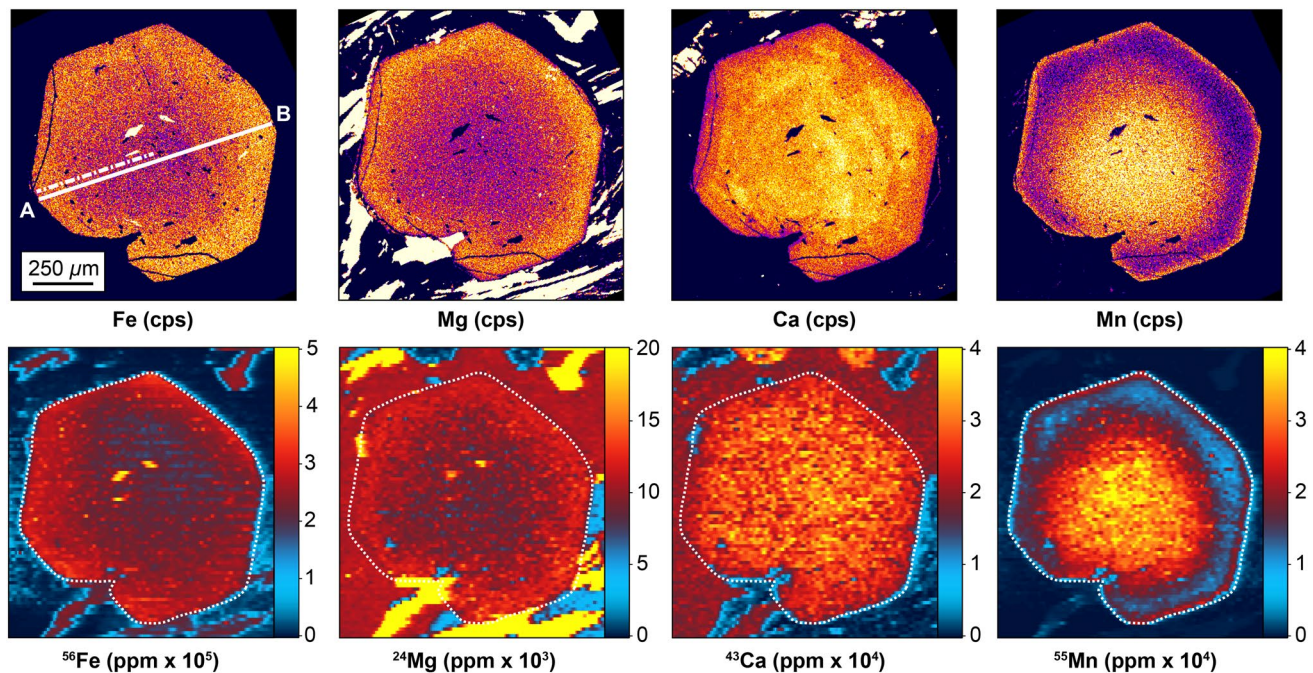
Fig. 4 Comparison between EPMA and LA-ICP-MS major element maps from sample PH2-E. EPMA maps (*top*) indicate counts per second (cps) X-ray abundances (see Fig. 8 of Raimondo et al. 2012). Quantified LA-ICP-MS maps (*bottom*) show ppm abundances. *Warmer* colours represent higher concentrations, and *colour scales* have been adjusted to highlight intragrain variability in garnet. *Dashed line* represents the grain boundary outline of the garnet crystal. LA-ICP-MS data extracted parallel to line A–B are presented in Figs. 6 and 7, and *dash–dot line* represents the position of the core–rim REE profile shown in Fig. 12. Note that the direction of laser travel is from *left* to *right* in all images, and pixel sizes are approximately 7 × 16 μm

inclusions (see Ce, Zr, Th, and U maps in Fig. 5), but the most significant feature is a dramatic LREE enrichment at the grain boundary coincident with a spike in Mn. This is particularly apparent on the Ce map and in the LREE line profiles (Fig. 6), with concentrations reaching ~800 ppm for Ce and ~100 ppm for La and Nd. Ce 'hotspots' in the rim domain are matched by peaks in Th (60–115 ppm); this is also true of a linear fracture in the upper part of the grain that extends from core to rim (white arrows on Ce and Th maps in Fig. 5). Finally, ilmenite inclusions apparent on the Fe map are also highlighted by Ti hotspots.

The variable distribution of REEs in different intragrain domains of PH2-E is further highlighted by the composite RGB image (Fig. 5). This comprises Ce as the red channel (representing LREEs concentrated in rim areas and along fractures), Gd as the green channel (representing MREEs concentrated in outer annuli), and Lu as the blue channel (representing HREEs concentrated in central and satellite peaks).

Sample PH4

Similar to PH2-E, LA-ICP-MS major element maps from PH4 (Fig. 8) show good agreement with EPMA X-ray maps from the same sample. The distinctive garnet mosaic texture is highlighted by concentric core-to-rim variations in Mg and Mn across large grain fragments, whereas smaller fragments are more homogeneous. Fe exhibits less pronounced zoning, only visible at the margins of the largest grain fragments, whereas Ca is essentially flat across all fragments regardless of size except for thin zones of Ca enrichment along fracture networks. Note that the broad gradient in the EPMA Fe map is due to a geometry effect related to electron beam defocussing, caused by slight tilting of the sample surface over a large area, and hence is not apparent on the LA-ICP-MS map.

To an even greater extent than PH2-E, the trace element zoning patterns of PH4 (Fig. 9) appear dissimilar to that of the major elements. The most noticeable contrast is the distribution of HREEs, which show continuous trends uninterrupted by the grain boundaries of adjacent fragments to create a smoothly varying radial pattern across the entire garnet mosaic. As shown along line C–D (Fig. 10), PH4 does not exhibit the same annular structure as PH2-E, with evenly distributed decreasing trends for all REEs. Nevertheless, there is some evidence of HREE enrichment at the outer margins of grain fragments that is matched by a spike in Mn, LREEs, and MREEs, a feature most prominent where they are in direct contact with matrix biotite (e.g., white arrow on Tm and Yb maps in Fig. 9; right-hand edge
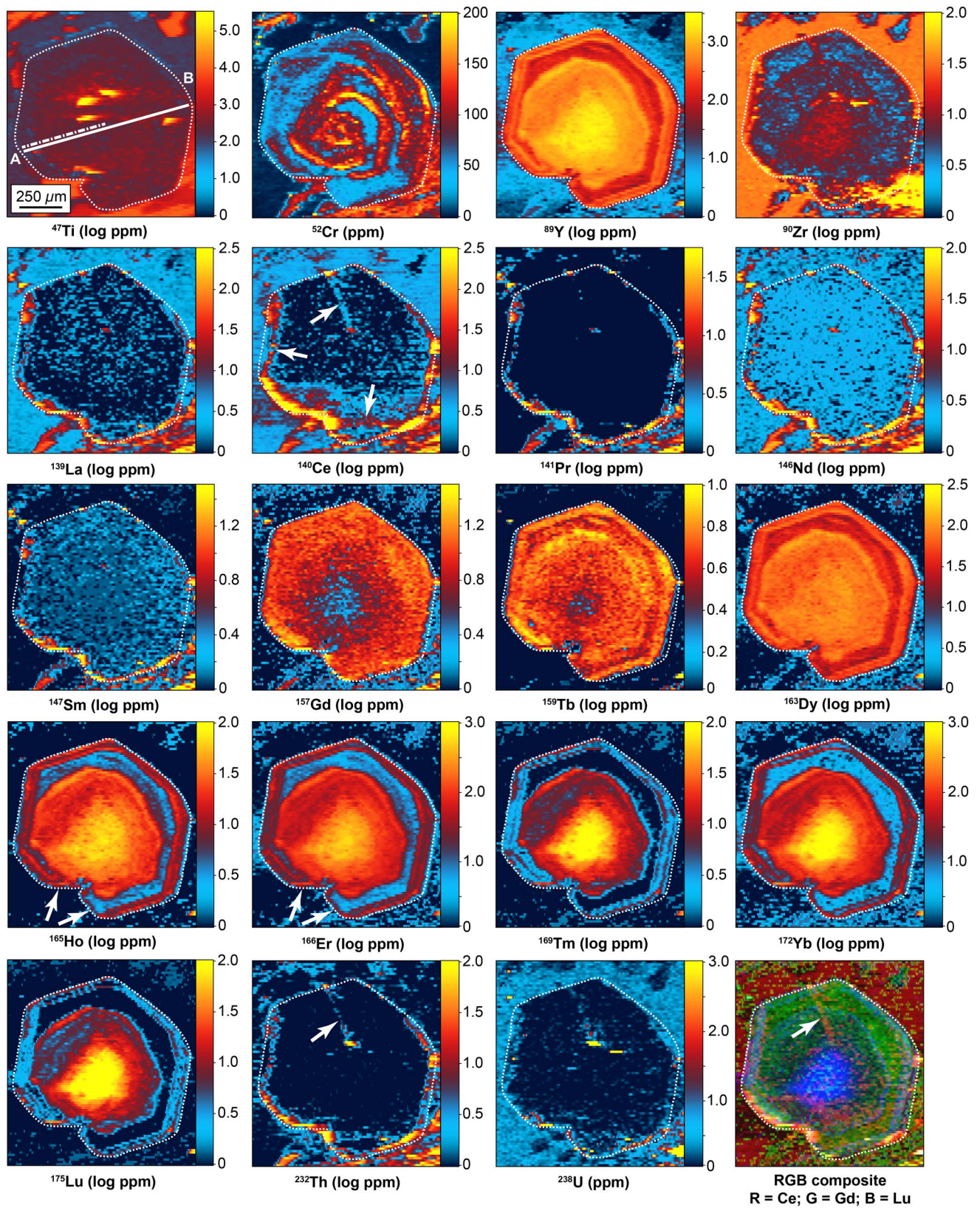
^{47}Ti (log ppm)

^{52}Cr (ppm)

^{89}Y (log ppm)

^{90}Zr (log ppm)

^{139}La (log ppm)

^{140}Ce (log ppm)

^{141}Pr (log ppm)

^{146}Nd (log ppm)

^{147}Sm (log ppm)

^{157}Gd (log ppm)

^{159}Tb (log ppm)

^{163}Dy (log ppm)

^{165}Ho (log ppm)

^{166}Er (log ppm)

^{169}Tm (log ppm)

^{172}Yb (log ppm)

^{175}Lu (log ppm)

^{232}Th (log ppm)

^{238}U (ppm)

RGB composite
R = Ce; G = Gd; B = Lu

◄**Fig. 5** Quantified LA-ICP-MS trace element maps from sample PH2-E. All maps show log ppm abundances to accentuate zoning, excluding Cr and U (ppm abundances). *Warmer colours* represent higher concentrations, and *colour scales* have been adjusted to highlight intragrain variability in garnet. *Dashed line* represents the grain boundary outline of the garnet crystal. LA-ICP-MS data extracted parallel to line A–B are presented in Figs. 6 and 7, and *dash–dot line* represents the position of the core–rim REE profile shown in Fig. 12. *White arrows* refer to features described in the text. Note that the direction of laser travel is from *left* to *right* in all images, and pixel sizes are approximately 7×16 µm

of line E–F in Fig. 10). Fragments adjacent to other matrix minerals (primarily quartz) show no HREE spikes (e.g., line C–D in Fig. 10). Isolated HREE hotspots correspond to zircon grains concentrated along fracture networks as indicated by comparison with the Zr map.

LREE and MREE patterns are partially obscured by significant spikes along fracture networks, many of which host monazite grains (see hotspots in Ce map; Fig. 9). Broad areas of elevated values around such accessory minerals are caused by smearing effects (see "Discussion"). However, whereas most LREE maps have ppm values near zero and appear generally flat, there remain subtle intragrain zoning profiles adjacent to grain boundaries for MREEs such as Sm, Gd, and Tb (white arrows in Fig. 9; line C–D in Fig. 10). Importantly, the increases in Sm and Gd do not occur along the margins of all fragments that comprise the garnet mosaic, but rather are confined to regions that probably constituted the grain boundary of the originally contiguous garnet fragments prior to fracturing. These features are largely mimicked by the Tb map, which also exhibits a subtle core and rim structure reminiscent of the remaining HREEs, and highlighted further by the composite RGB image comprising La (red channel), Gd (green channel), and Lu (blue channel). Finally, significant intragrain variations in trace elements such as Zr and Ti are essentially absent across the entire garnet mosaic.

Discussion

General comments on the acquisition of LA-ICP-MS trace element maps

Signal smearing

Before interpreting the significance of zoning patterns revealed by LA-ICP-MS mapping, it is important to consider several factors that influence the quality of data acquired by this technique. Perhaps the most obvious shortcoming is the lateral smearing of features in the direction of scanning (from left to right in the present case). For example, note the smearing of ilmenite inclusions on the

Ti map of sample PH2-E (Fig. 5), and similarly, the slightly sharper appearance of the left-hand edge of each annulus compared to its right-hand edge on the HREE maps. Sample PH4 most noticeably shows a smearing effect adjacent to zircon and monazite grains, coincident with a dramatic spike in Zr and Ce abundance (Fig. 9).

There are two major factors that contribute to signal smearing, both ultimately due to the problem of redeposition. First, ablated material can accumulate in linear ridges at the margins of raster trenches (Fig. 3), causing it to become incorporated into subsequent rasters and contaminate the sample volume. This issue can be effectively reduced by pre-ablation of each scan to remove excess material not originally evacuated from the cell, eliminating cross-raster contamination. However, it cannot combat continuous redeposition in front of the advancing ablation zone during each scan; signal smearing in the direction of travel can still occur even if lateral smearing onto adjacent rasters is eliminated by pre-ablation. Second, refractory elements (e.g., REEs, Ti, and Zr) that are significantly above background can cause large spikes with slow signal decay due to the washout characteristics of the sample cell. Their high melting points cause the formation of large aerosol droplets that become redeposited and prevent rapid cell evacuation.

The overall impact of smearing artefacts is to exaggerate the size of inclusions, grain boundaries, or intragrain domains, and to blur interfaces characterised by sharp changes in abundance. Consequentially, some caution needs to be exercised when interpreting the spatial properties of such features, particularly the precise length scales of compositional profiles across interfaces or the false 'halo' effects around accessory minerals. This is especially true for line profiles constructed parallel to the raster direction. Signal smearing is also more pronounced for low-abundance refractory elements than major elements. The latter are thus better choices to define the true compositional profiles and spatial extent of intragrain interfaces and grain boundaries (particularly their right-hand margins), bearing in mind that any redeposition inherently produces partial decoupling across the entire suite of analysed elements depending on their specific ablation characteristics.

Spatial resolution and accuracy

A second deficiency of LA-ICP-MS mapping is the compromise involved in pixel creation. All trace element maps presented in Figs. 5 and 9 have rectangular pixels that are approximately twice as long in the *y*-direction (perpendicular to the raster) as the *x*-direction (parallel to the raster). The former is dependent on the laser spot size and line separation, which are kept equal to avoid overlap or mismatch between successive rasters and create a seamless image. In contrast, the latter is dictated by the laser scan
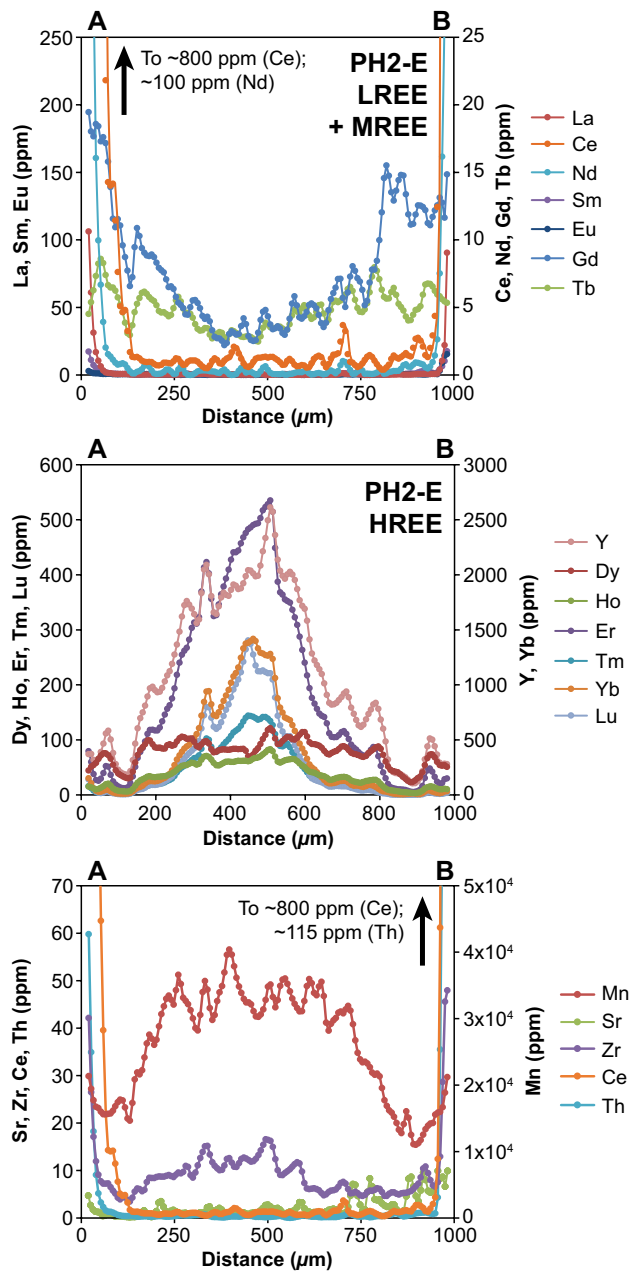
Fig. 6 LA-ICP-MS ppm values across line *A–B* indicated in Figs. 4 and 5 for sample PH2-E. Profiles are extracted from the stitched raster data using the *XMapTools* line mode sampling function

speed and integration interval used for data processing. *Iolite* generates discrete data from the time-resolved integration of each signal, as determined by the time required for the mass spectrometer to sweep through the entire mass range being measured. Hence, the pixel size in the *x*-direction is determined by the relationship between the sum of the dwell times on individual isotopes and the distance traversed along the raster during this interval.

Competition between the increased mass range of the LA-ICP-MS technique and the time required for sequential

acquisition of large element suites has important implications for the spatial resolution and referencing of maps acquired by this method. First and foremost, LA-ICP-MS maps are inherently different to conventional EPMA X-ray maps, because all masses are not measured simultaneously on separate spectrometers. Rather, they are measured successively with the extent of signal decoupling determined by the cumulative dwell time (i.e., in the present case, a low mass element is measured 0.31 s before a high mass element on the same mass sweep). Combined with the potential redeposition effects discussed previously, this implies that successive masses do not share precisely the same spatial reference. If more masses are added to the sweep or dwell times are increased to improve total counts, the extent of decoupling becomes greater; hence, this parameter needs to be optimised to balance the elements of interest with the spatial resolution required.

Nevertheless, for the sweep times used in this study, such differences are small enough to produce meaningful maps given the high sensitivity of modern mass spectrometers and the fast repetition rates employed. Of greater concern for map accuracy are the following: (1) zoning features or interfaces can incorrectly appear as mixed compositions where the length scale of change is smaller than the spatial resolution of adjacent pixels; and (2) the continuity of data between successive rasters is dependent on the precision and reproducibility of stage positioning. For the instrument conditions used in this study (16 μm spot size, 22 μm s^{-1} scan speed, 0.31 s total sweep time), the pixel sizes are approximately 7×16 μm. Although inferior to the spatial resolution of typical EPMA X-ray maps, this is satisfactory to distinguish gradational zoning transitions larger than two successive pixels (i.e., > 14 μm laterally and > 32 μm vertically; note the fine satellite peaks resolved in REE maps of sample PH2-E in Fig. 5). Greater numbers of successive pixels will be required to define chaotic or patchy zoning patterns and avoid compositional mixing. Smaller spot sizes enable greater resolution and image pixels to become approximately equidimensional, but at a cost of poorer count rates and hence decreased detection limits. For detecting REE distributions in garnet, our experience shows that typical mafic rock compositions may require larger spot sizes due to generally lower counts, whereas pelitic rocks such as those used in this study produce acceptable results at smaller spot sizes.

Origins and timing of major and trace element distributions in garnet

Sample PH4: retention and resetting of inherited growth zoning during metasomatism and resorption

The Peaked Hill samples provide several insights into the origins of contrasting trace element distributions in garnet

Fig. 7 Stacked line profiles using the LA-ICP-MS ppm data pre- ▶
sented in Fig. 6 for sample PH2-E, with vertical offset between each
element for clarity. Note the transition from bell- to bowl-shaped
profiles for HREEs vs LREEs. *Dashed lines* indicate the correlation
between the radial positions of superimposed peaks. Slight peak mis-
matches noticeable for LREEs are due to smearing effects, low abun-
dances at or near detection limits (see Fig. 6), or minor signal decou-
pling due to the cumulative dwell time delays in each mass sweep

and their geological significance. Perhaps most strikingly,
PH4 demonstrates the complete decoupling of major and
trace element mobility through superimposed events. As
illustrated in Fig. 2 and outlined by Raimondo et al. (2012),
the garnet mosaic comprises originally contiguous frag-
ments that were fractured during shearing, whilst retain-
ing elongate grain shapes and fibrous sillimanite inclu-
sions diagnostic of garnets inherited from the adjacent wall
rocks. Granulite facies metamorphism of the wall rocks is
attributed to the 1600–1530 Ma Chewings Orogeny (Vry
et al. 1996; Williams et al. 1996; Rubatto et al. 2001; Mor-
rissey et al. 2014), whereas later overprinting and meta-
somatism is dated at c. 360 Ma (Alice Springs Orogeny)
by monazite inclusions in matrix biotite (Raimondo et al.
2012). Despite (1) an approximately 1200 Myr age differ-
ence between the sheared rocks and their gneissic precur-
sor; (2) the complete flattening of major element zoning in
granulitic garnets (see Fig. 7 of Raimondo et al. 2012); and
(3) their subsequent disintegration and diffusional resetting
to produce radial major element zoning in individual grain
fragments, the record of original prograde growth zoning is
still preserved by a bell-shaped REE distribution that tran-
sects the entire garnet mosaic (Fig. 9).

Such remarkable retention of PH4's trace element
archive demonstrates its overall lack of responsiveness to
high-grade metamorphism and deformation. The Chewings
Orogeny sustained high-*T*, low-*P* suprasolidus conditions
for >80 Myr, with peak conditions in excess of 850 °C at
6.5–7.5 kbar (Anderson et al. 2013; Morrissey et al. 2014;
Huston et al. 2016). The Alice Springs Orogeny involved
multiple episodes of deformation and metamorphism over
a duration of 150 Myr from 450 to 300 Ma (Haines et al.
2001; Buick et al. 2008; McLaren et al. 2009; Raimondo
et al. 2014), with widespread fluid–rock interaction at
conditions of 550 °C and 5.0–6.5 kbar during its terminal
phase represented by the c. 360 Ma Peaked Hill samples
(Cartwright and Buick 1999; Raimondo et al. 2011, 2012;
Schoneveld et al. 2015). The pervasive fracturing and
communion of rigid garnet porphyroclasts during Alice
Springs shearing requires high differential stress to over-
come its high yield strength (e.g., Whitney et al. 2007;
Zhang and Green 2007), which may promote geochemical
mobility by increasing dislocation density and surface to
volume ratios (Austrheim et al. 1996; Terry and Heidelbach
2006). Similarly, the production of sub-grain boundaries
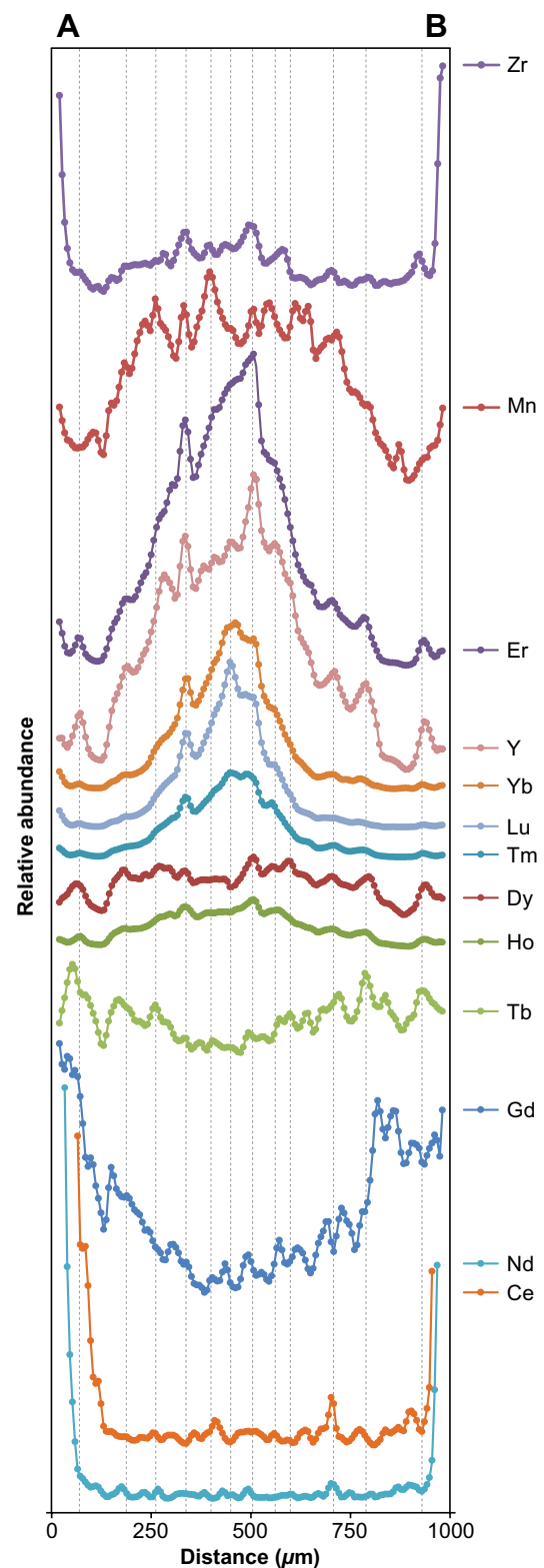
through dissolution processes should also promote dif-
fusive element exchange (Konrad-Schmolke et al. 2007).
Yet, through all of these superimposed events involving
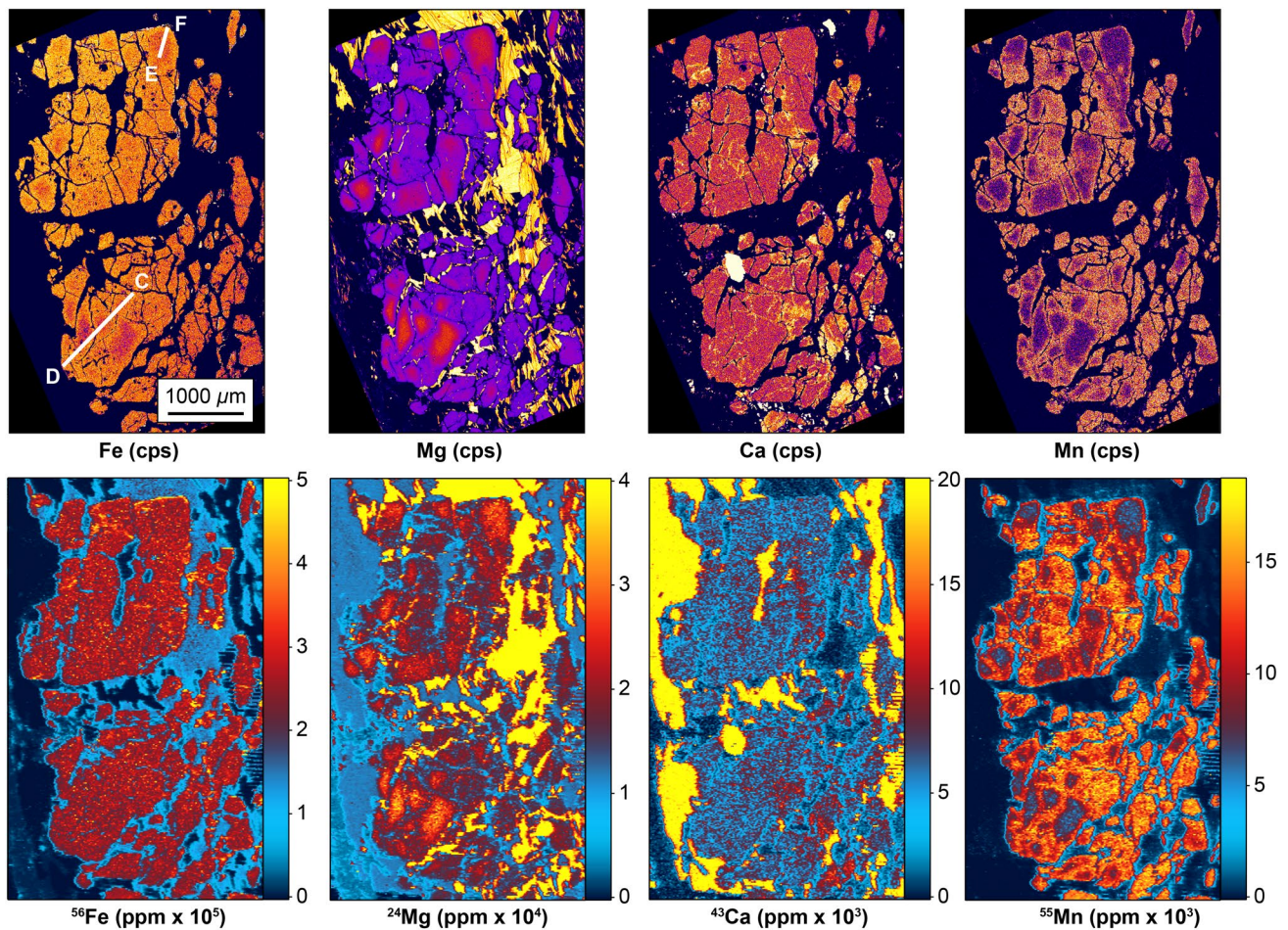prolonged and intense metamorphism and deformation,

Fig. 8 Comparison between EPMA and LA-ICP-MS major element maps from sample PH4. EPMA maps (*top*) indicate counts per second (cps) X-ray abundances (see Fig. 7 of Raimondo et al. 2012). Quantified LA-ICP-MS maps (*bottom*) show ppm abundances. *Warmer colours* represent higher concentrations, and *colour scales* have been adjusted to highlight intragrain variability in garnet. LA-ICP-MS data extracted parallel to lines *C–D* and *E–F* are presented in Fig. 10, and core–rim REE profile parallel to line *E–F* is shown in Fig. 12. Note that the direction of laser travel is from *left* to *right* in all images, and pixel sizes are approximately 7×16 µm

and notwithstanding the wholesale diffusional relaxation and later rock-wide intergranular re-equilibration of major elements, the original REE growth zoning is largely unaffected.

Nevertheless, some evidence remains of limited REE mobility. Modified HREE zoning is apparent at grain boundaries in direct contact with matrix biotite, coincident with elevated $\delta^{18}O$ values identified by in situ SIMS analyses (Raimondo et al. 2012). A strong correlation with spikes in Mn, LREEs, and MREEs (Fig. 10) suggests that local enrichment was facilitated by intragranular back-diffusion during garnet dissolution. The existence of broad, linear zones marked by discrete shifts in Sm, Gd, and Tb along the former garnet rim (Figs. 9, 10) also attests to modification of the inherited REE distribution via a similar mechanism. The continuity of Sm, Gd, and Tb peaks across several grain fragments indicates that dissolution initiated prior to fracturing of the relict garnet, and hence deformation was comparatively late in the metamorphic sequence. Importantly, the existence of Mn spikes encircling the individual mosaic fragments of PH4 (Fig. 8), along with similar Mn enrichment at the outermost rim of PH2-E (Fig. 4), demonstrates the occurrence of an additional resorption event that postdates deformation. We therefore speculate that the initial (pre-deformation) breakdown of relict garnets such as PH4 may have scavenged HREEs for the growth of new porphyroblastic garnets such as PH2-E (Fig. 11), whereas subsequent resorption produced inward diffusion of all REEs at matrix biotite interfaces.

Sample PH2-E: equilibrium growth zoning with changes in the major mineral assemblage

Despite being part of the same shear zone and sampled within metres of each other, garnets from sample PH2-E

are evidently not inherited from the adjacent granulite wall rocks in the same way as sample PH4. Rather, their euhedral shape and lack of sillimanite inclusions (Fig. 2), coupled with concentric major and trace element zoning, suggest that they grew in response to metasomatism during the Alice Springs Orogeny. This interpretation is confirmed by an Sm–Nd isochron age of c. 330 Ma (Raimondo et al. 2012), and enables a comparison between major and trace element mobility associated with prograde growth as opposed to dissolution and disaggregation of relict grains.

Convoluted Cr zoning in PH2-E highlights an irregularly-shaped core domain that appears to be overgrown by a euhedral rim (Fig. 5). This internal structure is also evident in the REE maps (particularly Lu, Yb, and Tm), which show a series of asymmetric annuli. Vague patchiness in the EPMA Ca map appears to be the only correlative to the 'spiral' structure seen in Cr, perhaps indicating that their distributions are linked to coupled cation substitution. Importantly, each of these features is largely absent from the EPMA major element maps and would be easily missed by the conventional 1D trace element profiles, demonstrating the considerable improvements to paragenetic context that are gained via 2D LA-ICP-MS mapping.

Radial REE zoning in PH2-E follows the distribution predicted by reaction-controlled matrix equilibration during garnet growth (Hickmott and Spear 1992; Pyle and Spear 2003; Konrad-Schmolke et al. 2008), where dominant central peaks for HREEs are followed by less pronounced peaks and annular maxima for MREEs, and high annular maxima for LREEs (Figs. 5, 6). This model is analogous to the diffusion-limited mechanism proposed by Skora et al. (2006), but with two key differences: (1) a narrow central peak is absent for LREEs and some MREEs; and (2) there is no REE peak displacement towards the rim with decreasing atomic number. Whereas the former may be caused by non-central section failing to intersect the true garnet core (or alternatively eradicated by volume diffusion), the latter condition eliminates any appeal to variable diffusion velocities to explain the REE distribution. Rather, it is indicative of relatively fast intergranular mobility and approximately rock-wide thermodynamic equilibrium.

Strong correlation between the radial positions of all superimposed peaks shown by PH2-E (Figs. 6, 7) suggests that sequential changes in nutrient availability affected all REEs simultaneously. Consistent with the model of Konrad-Schmolke et al. (2008), this argues for REE uptake being controlled by continuous adjustments to the garnet-forming reaction during prograde growth, without significant diffusional limits as is usually indicative of hydrous conditions (Skora et al. 2006; Moore et al. 2013). As the reaction path is followed, matrix minerals are progressively depleted in HREEs and enriched in LREEs relative to garnet due to differences in element compatibility. Bell-shaped

HREE distributions are thus controlled by bulk rock depletion and Rayleigh fractionation into the growing garnet. In contrast, as later mineral breakdown reactions liberate increasing amounts of LREEs according to predicted garnet/matrix partition coefficients, there is a transition to bowl-shaped zoning profiles where annular maxima reflect equilibration with the evolving matrix assemblage.

Note that this REE distribution is subtly different to that of PH4 (Figs. 9, 10), which contains smooth core-to-rim variations and no annular maxima regardless of atomic number, typical of Rayleigh fractionation (Hollister 1966; Otamendi et al. 2002; Tirone et al. 2005). This is consistent with nucleation at high temperature, where rapid intergranular diffusion for all REEs relative to crystal growth prevents the development of diffusion gradients in the matrix and thus local fluctuations in REE uptake (Moore et al. 2013). Importantly, the absence of annular maxima suggests that the matrix assemblage was essentially unchanging during garnet crystallisation, and thus the effective bulk rock REE composition was continuously depleted by fractionation processes alone. The differential uptake of REEs according to Rayleigh fractionation vs reaction-controlled matrix equilibration is highlighted by scatter plots of REE concentrations illustrated in Fig. 11, and normalised REE diagrams shown in Fig. 12.

Relationship between garnet zoning and changes in the accessory mineral assemblage

Along with zoning characteristics influenced by major mineral reactions, the existence of several superimposed REE spikes in rim domains of PH2-E (Figs. 5, 6) indicates that the latter stages of garnet growth and dissolution were influenced by successive changes in the accessory mineral assemblage. The most prominent features are the double satellite peaks marked by significant enrichments in HREEs. The inner satellite peak is matched by a spike in Zr, suggesting that it represents the breakdown of zircon grains inherited from the granulite wall rock. As shown in Fig. 5, the whole-rock Zr budget is dominated by zircon, with a single grain producing the broad smear evident in the lower right-hand corner of the Zr map, and similar hotspots littering the Zr map of sample PH4 (Fig. 9). The breakdown of major matrix minerals is thus an unlikely source of Zr + HREE enrichment.

The inner satellite peak is succeeded by a dramatic increase in LREE abundance at the outermost rim. LREE enrichment is most pronounced at embayed sections of the grain boundary in direct contact with matrix biotite (Figs. 5, 6). Coincident Ce, Th, and Mn spikes suggest that the outer satellite peak represents monazite breakdown during garnet resorption, and truncation of the inner satellite peak along the embayment suggests that
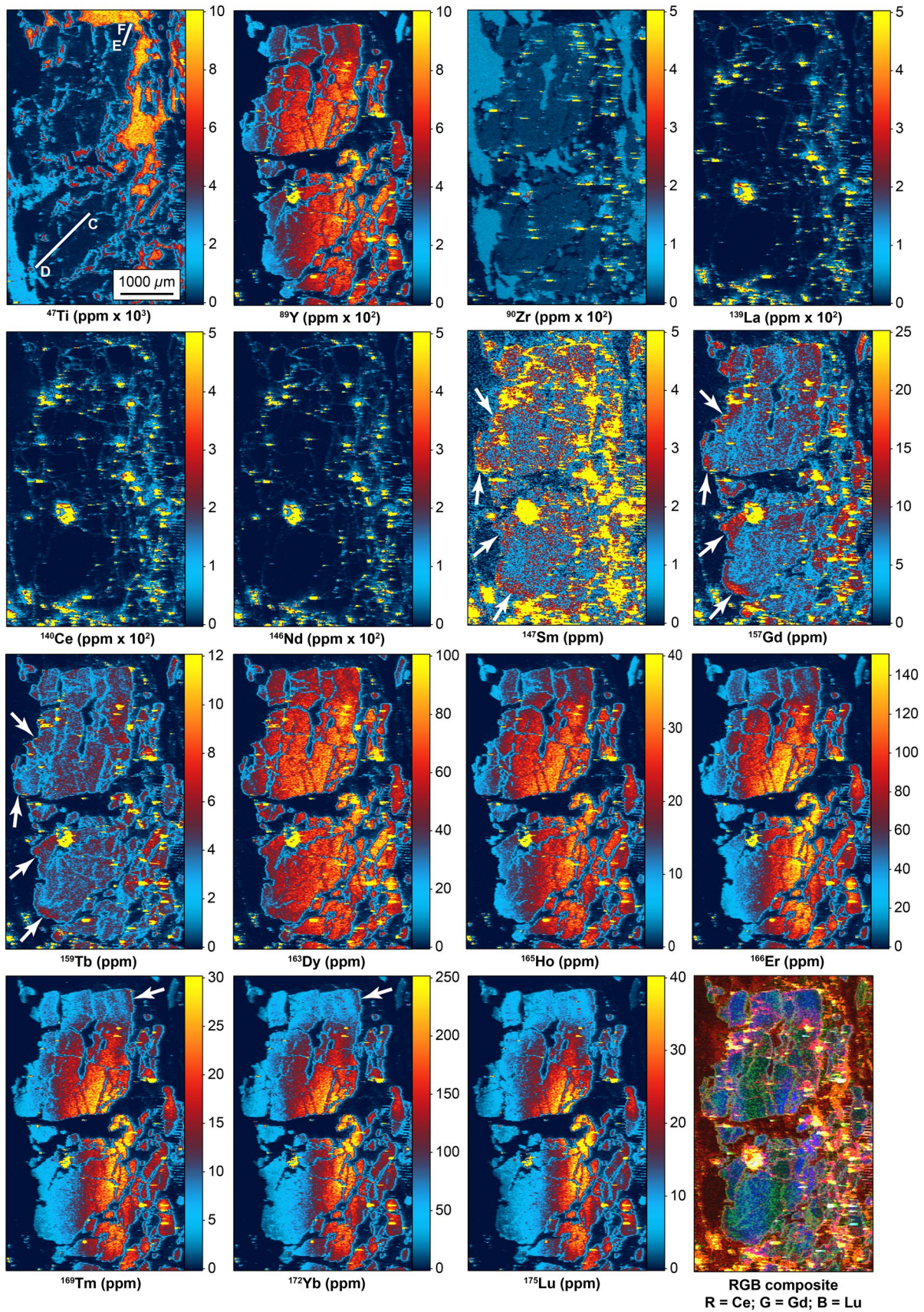
◀**Fig. 9** Quantified LA-ICP-MS trace element maps from sample PH4. All maps show ppm abundances. *Warmer colours* represent higher concentrations, and *colour scales* have been adjusted to highlight intragrain variability in garnet. LA-ICP-MS data extracted parallel to lines *C–D* and *E–F* are presented in Fig. 10, and core–rim REE profile parallel to line *E–F* is shown in Fig. 12. *White arrows* refer to features described in the text. Note that the direction of laser travel is from *left* to *right* in all images, and pixel sizes are approximately $7 \times 16\ \mu m$

this feature represents earlier zircon breakdown prior to resorption. Equivalent to the ubiquitous LREE hotspots evident in PH4 (Fig. 9), the whole-rock LREE budget of PH2-E is dominated by monazite, as illustrated in Fig. 2b. Plagioclase breakdown may be an alternative explanation for LREE availability, but concomitant increases in feldspar-hosted LILEs such as Sr are not observed, as opposed to marked increases in incompatible HFSEs such as Th (Fig. 6). Reduction of the negative Eu anomaly is also absent despite a strong increase in the positive Ce anomaly (Fig. 12). Hence, given that core domains of monazite grains return an age of 354 ± 3 Ma (Raimondo et al. 2012), it is interpreted that coupled monazite and garnet breakdown commenced subsequent to this time during the waning phases of the Alice Springs Orogeny. Similar to PH4, this argues for enhanced mobility of

REEs (and O) during retrograde dissolution–reprecipitation reactions, most likely promoted by alkali-bearing metasomatic fluids that increase monazite and zircon solubility and permit Ce oxidation to its more compatible tetravalent state (Rubatto et al. 2008; Putnis 2009; Hetherington et al. 2010; Harlov et al. 2011; Ayers et al. 2012; Wilke et al. 2012).

Finally, PH2-E shows some evidence for enhanced LREE mobility along fracture networks. The Ce map reveals two linear features with elevated values (white arrows in Fig. 5) that correspond to penetrative fractures on the EPMA major element maps (Fig. 4). There is also a noticeable streak extending from the upper grain boundary to the centre of the grain, again marked by LREE enrichment that is apparent as a red stripe on the composite RGB image (Fig. 5). Discrete channelling along open fractures suggests that spatially restricted LREE exchange occurred via a similar mechanism to coupled oxygen-cation interdiffusion, as a consequence of increased fluid access, chemical potential gradients and reactive surface areas along these pathways (e.g., Erambert and Austrheim 1993; Hames and Menard 1993; Whitney 1996; Konrad-Schmolke et al. 2007; Putnis and Austrheim 2010).

Fig. 10 LA-ICP-MS ppm values across lines *C–D* and *E–F* indicated in Figs. 8 and 9 for sample PH4. Gaps along line *C–D* represent excluded data due to either the presence of inclusions or grain boundaries being crossed between adjacent garnet fragments. Profiles are extracted from the stitched raster data using the *XMapTools* line mode sampling function
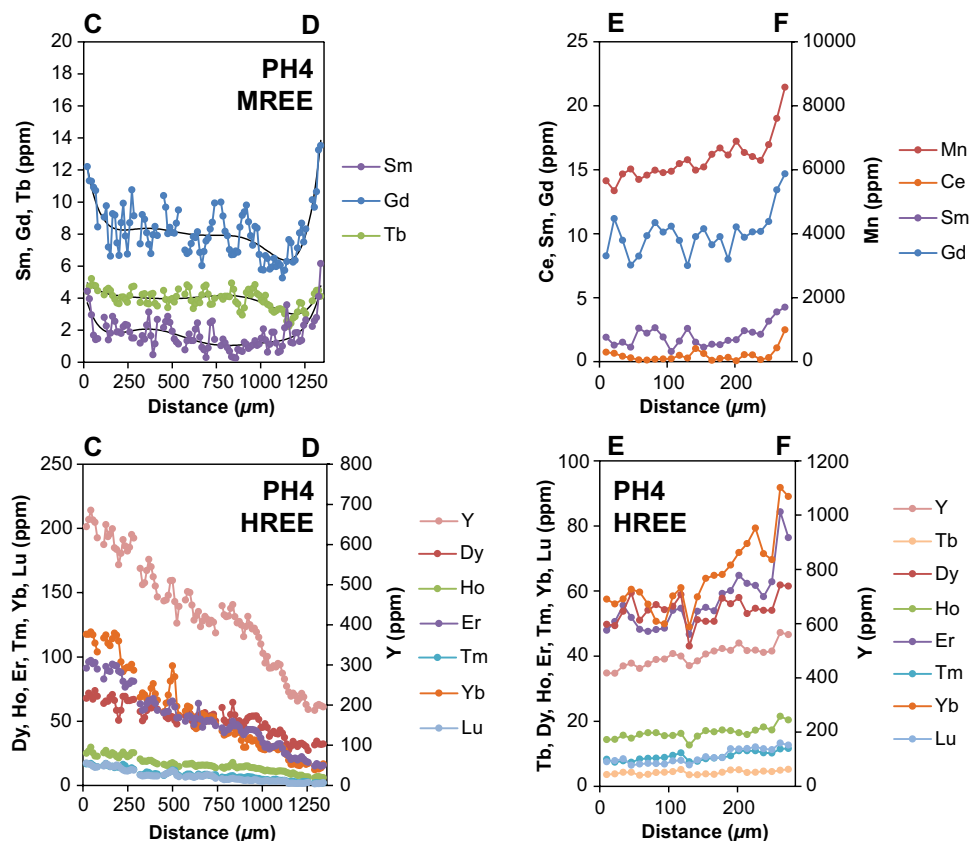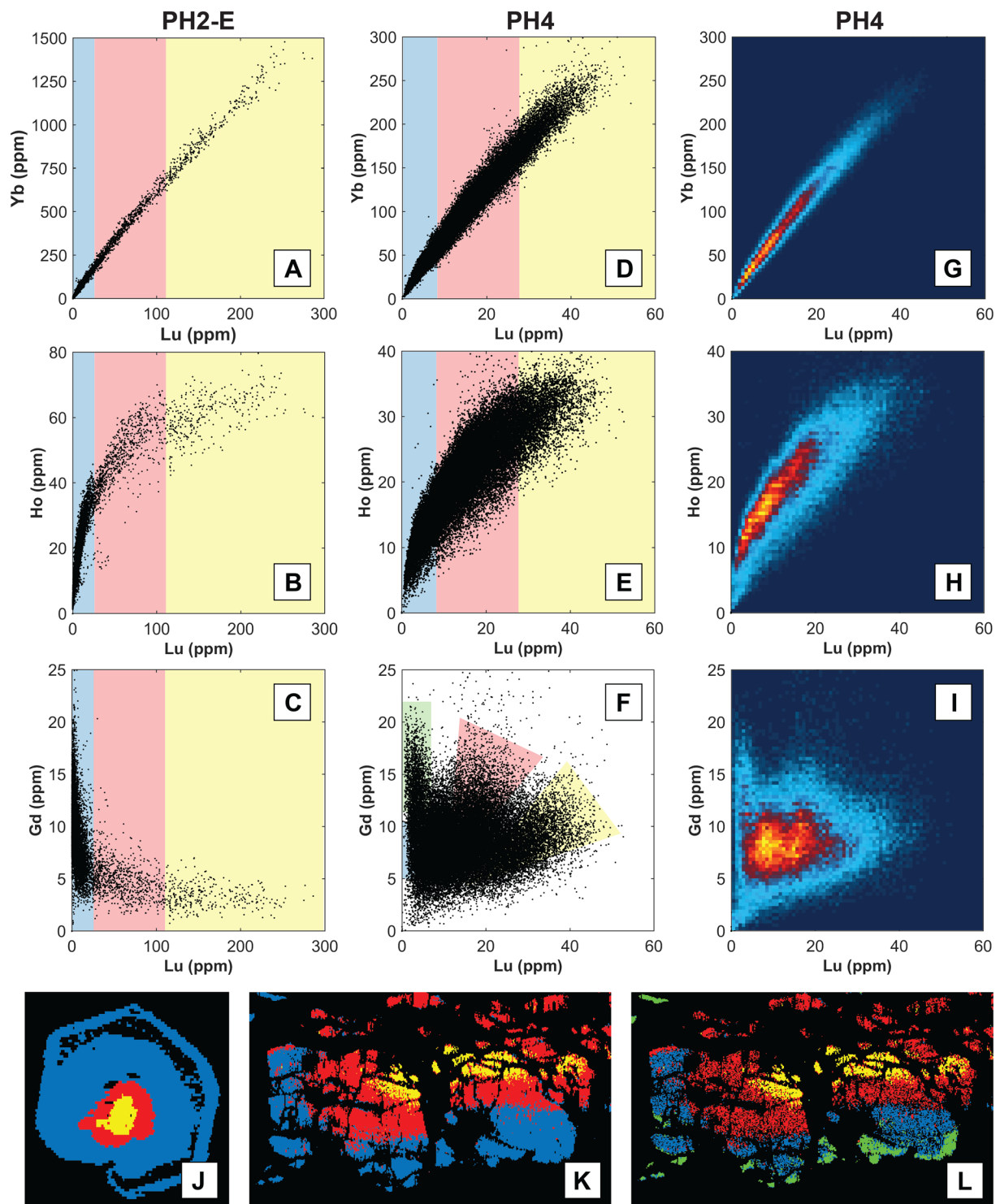
Implications for U–Pb, Sm–Nd and Lu–Hf geochronology

LA-ICP-MS trace element mapping provides a powerful means to directly link garnet evolution to temporal constraints provided by accessory mineral geochronometers. The interpretation of U–Pb geochronology is assisted by the identification of changes to key geochemical reservoirs that host REEs and other trace elements, manifested as dramatic increases or decreases in the availability of these nutrients to garnet nucleation sites and/or domains undergoing diffusional exchange. As described above, the superposition of spikes and satellite peaks can be correlated with either the growth or breakdown of zircon and monazite,

◄**Fig. 11** Binary scatter plots of Yb, Ho, and Gd concentrations plotted against Lu for **a–c** sample PH2-E and **d–f** sample PH4, showing the variation in REE zoning characteristics according to atomic number. Density maps calculated from each scatter plot for PH4 are shown in **g–i**; equivalent density maps for PH2-E are not shown because they exactly replicate their corresponding scatter plots. Note the strong correlation between Lu vs Yb in PH2-E that becomes progressively weaker for Lu vs Ho and Lu vs Gd, consistent with variable REE availability due to reaction-controlled matrix equilibration and garnet/matrix partitioning relationships. In contrast, PH4 shows a broadly linear correlation for all REEs that approximates Rayleigh fractionation, with progressive broadening and anticlockwise rotation of the scatter corresponding to an incremental reduction in HREE (Lu) vs MREE (Gd) concentrations as garnet grows with an unchanging matrix assemblage. Smooth variations in REE concentrations from core to rim indicate gradual depletion of the REE reservoir as temperature increases along the prograde path. *Coloured shading* in plots **a–f** corresponds to the intragrain domains indicated in the pixel identification maps below: diagrams **a–c** relate to map **j**, diagrams **d, e** to map **k**, and diagram **f** to map **l**. The *blue box* in **f** is the same width as the *green box* directly above but largely obscured by data points. Note the discrete cluster of points where Gd is decoupled from Lu in PH4, corresponding a zone of garnet resorption prior to fracturing highlighted by green pixels in **l**. MREEs such as Gd are back-diffused into the pre-existing granulitic garnet resulting in a concentration increase, whereas HREEs such as Lu are available to newly-grown garnet porphyroblasts such as PH2-E resulting in a concomitant concentration decrease

with similar principles applying to any other mineral of use for geochronology (e.g., rutile, titanite, apatite, allanite, etc). Furthermore, the ability to measure a large suite of REEs and trace elements such as U, Th, Pb, Zr, P, and Ti means that the discrimination of multiple accessory minerals is readily achieved. Combined with petrographic observations, *P–T* pseudosection modelling and additional microanalytical data sets (e.g., EPMA major element maps and SIMS oxygen isotope traverses), detailed paragenetic sequences can thus be constructed to reveal in new detail the step-by-step evolution of mineral assemblages (e.g., Pyle and Spear 2003; Yang and Pattison 2006; Corrie and Kohn 2008; Konrad-Schmolke et al. 2008; Kelsey and Powell 2011; Raimondo et al. 2013; Dumond et al. 2015).

Further temporal information can also be provided by direct dating of garnet itself through the application of Sm–Nd and Lu–Hf geochronometers. Both isotope systems can yield precise ages to constrain the duration of mineral growth and/or diffusional modification, with improved sampling resolution via micromill or microsaw techniques in some cases allowing the differentiation of events <1 Ma in duration (e.g., Pollington and Baxter 2011; Dragovic et al. 2015; Schmidt et al. 2015). However, the validity of age estimates provided by garnet geochronology is crucially dependent on an understanding of the REE distribution and its impact on ^{176}Lu/^{177}Hf and ^{147}Sm/^{144}Nd ratios (e.g., Lapen et al. 2003; Skora et al. 2006; Konrad-Schmolke et al. 2008; Kohn 2009; Kelly et al. 2011). Many workers have emphasised this point repeatedly, but recent studies

have revealed in greater detail the potential for dramatic age differences caused by the interplay between growth and diffusion rates during nucleation, or due to post-growth modification via resorption (Anczkiewicz et al. 2007, 2012; Cheng et al. 2008; Dutch and Hand 2010; Kelly et al. 2011; Smit et al. 2013). In addition, REE zoning has a crucial impact on isochron precision, and REE abundance may influence the preferential retention of daughter vs parent nuclides due to faster diffusion at low net concentrations (Bloch and Ganguly 2015; Bloch et al. 2015).

The above points re-emphasise the value of LA-ICP-MS mapping to properly consider REE zoning in garnet and screen for samples likely to give meaningful ages. Whereas REE spot analyses are now considered essential for interpreting Sm–Nd and Lu–Hf isochrons, trace element maps offer a more robust method for examining their 2D spatial distribution and correlating with features such as overprint zoning, annular maxima, or satellite peaks (cf. Moore et al. 2013). These principles are aptly demonstrated by PH2-E, which exhibits a substantial spike in LREEs (including Nd) at its bottom edge (Figs. 5, 6, 12) that could easily be missed by linear traverses positioned closer to the top edge. Despite the narrow width of this zone (~100 μm at its widest), its position at the outermost rim means that it occupies a comparatively large portion of the total garnet volume. In effect, the accumulation of non-radiogenic Nd produces unusually low ^{147}Sm/^{144}Nd ratios, with the majority being <0.15 (Raimondo et al. 2012). This makes the apparent age younger and dramatically reduces isochron precision, as evidenced by an age uncertainty of ±20 Ma (95% confidence). Importantly, as noted by Raimondo et al. (2012), the identification of LREE peaks at the garnet rim is consistent with both leached and unleached fractions being in isotopic equilibrium, and rules out Nd enrichment being caused by unequilibrated mineral contaminants (Zhou and Hensen 1995; Scherer et al. 2000; Thöni 2002).

Summary and conclusion

The contrasting elemental distributions revealed by LA-ICP-MS mapping highlight the complexity of geochemical mobility in garnet through multiple superimposed events. This study examines the variable uptake and resetting of major and trace elements by processes ranging from high-temperature metamorphism and intense deformation to pervasive metasomatism and retrograde resorption. Our key observations are as follows:

- Growth zoning at high temperature and with an unchanging matrix assemblage is characterised by radial REE distributions independent of atomic number, produced by rapid intergranular diffusivities relative to
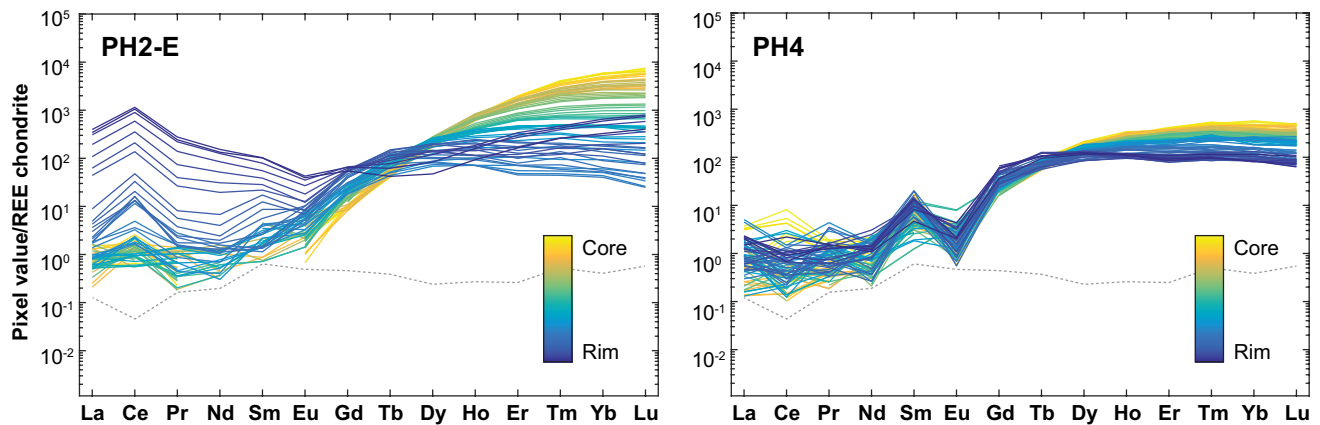
Fig. 12 Chondrite-normalised rare-earth element (REE) patterns for samples PH2-E and PH4, showing the variation in REE concentrations from core to rim across each garnet grain. For PH2-E, note the progressive HREE depletion from core to rim, a subdued negative Eu anomaly, and dramatic REE enrichment at the rim that produces a pronounced positive Ce anomaly. For PH4, note the more restricted spread of HREE depletion from core to rim, along with a strong negative Eu anomaly that weakens at the outermost rim coincident with sharp Gd and Tb enrichment. The 'see-saw' pattern of inversely correlated LREEs vs HREEs from core to rim in PH2-E is diagnostic of garnet crystallisation under reaction-controlled matrix equilibration, as opposed to the general positive correlation in PH4 indicative of Rayleigh fractionation. Data are extracted from individual pixels of the LA-ICP-MS trace element maps and processed using the *Spider* module of *XMapTools*. LREE values show increased scatter where they approach the chondrite-normalised limit of quantification (LOQ) for each element (*dashed grey line*). Core–rim profile for PH2-E extends along the radius of line *A–B* indicated in Figs. 4 and 5, and PH4 profile is positioned parallel to line *E–F* in Figs. 8 and 9. Normalisation follows Taylor and McClennan (1985)

crystal growth that enable equilibrium with the matrix to be approached. This is exemplified by the smooth core-to-rim zoning shown by sample PH4, with central and approximately coincident maxima for all REEs typical of a Rayleigh fractionation process.

- Growth zoning under reaction-controlled matrix equilibration is marked by radial REE zoning that shows a transition from bell- to bowl-shaped profiles with decreasing atomic number. Strong correlation between the radial positions of superimposed peaks suggests that nutrient supply and diffusion velocities are essentially equivalent for all REEs, most likely indicative of hydrous conditions. Sample PH2-E exhibits this characteristic pattern, produced as a result of changes in element availability dictated by sequential garnet-forming mineral breakdown reactions, with annular maxima formed according to garnet/matrix REE partitioning relationships.

- Superimposed on these primary growth zoning patterns are satellite peaks correlated with changes to the accessory mineral assemblage. Growth or breakdown of REE reservoirs such as zircon and monazite produce large fluctuations in the availability of nutrients to nucleation sites. For PH2-E, specific accessory minerals are identified by coincident trace element peaks (Zr and HREEs for zircon; Ce, Th, and LREEs for monazite), allowing garnet evolution to be placed in a specific paragenetic context and integrated with temporal constraints provided by geochronometers. 2D mapping of REE distri-

butions also provides a more robust screening method for Sm–Nd and/or Lu–Hf dating, combined with a powerful means to assess the precision and significance of such ages once they are obtained.

- Satellite peaks are also linked to a reduction in garnet mode during retrograde dissolution. Typically, this results in intragranular back-diffusion of elements with negligible concentrations in matrix minerals relative to garnet, marked by sharp spikes in elements such as Mn and REEs at the outermost rim that progressively decline towards the core. This feature is found at the margins of both PH2-E and PH4.

- The continuity or discontinuity of resorption features across garnet fractures allows the timing of dissolution to be constrained with respect to deformation. We argue that two dissolution events are captured by the major and trace element zoning patterns of PH2-E and PH4. The first initiated prior to fracturing of PH4, characterised by the preservation of contiguous back-diffusion zones for elements such as Sm, Gd, and Tb. Subsequent major element re-equilibration and local REE enrichment at the outermost rims of individual garnet fragments in PH4 and newly-grown porphyroblasts in PH2-E indicates a second dissolution event that post-dates deformation.

Ultimately, the above points illustrate the complex and parallel controls on geochemical mobility in garnet. On the one hand, the preservation of growth zoning inherited

from the granulite precursor to sample PH4 demonstrates the remarkable resilience of REEs to resetting during subsequent metamorphism, metasomatism, and deformation. On the other hand, the modified zoning shown by both PH2-E and PH4 demonstrates that REEs can be responsive to dissolution and re-equilibration processes under certain conditions. These apparently conflicting records, revealed in new detail by LA-ICP-MS mapping, are reconciled by the balance between element fractionation, mineral reactions and partitioning, and the length scales of intergranular transport.

References

Ague JJ, Axler JA (2016) Interface coupled dissolution-reprecipitation in garnet from subducted granulites and ultrahigh-pressure rocks revealed by phosphorous, sodium, and titanium zonation. Am Mineral 101:1696–1699. doi:10.2138/am-2016-5707

Ague JJ, Carlson WD (2013) Metamorphism as garnet sees it: the kinetics of nucleation and growth, equilibration, and diffusional relaxation. Elements 9:439–445. doi:10.2113/gselements.9.6.439

Anczkiewicz R, Szczepanski J, Mazur S, Storey C, Crowley Q, Villa IM, Thirlwall MF, Jeffries TE (2007) Lu–Hf geochronology and trace element distribution in garnet: Implications for uplift and exhumation of ultra-high pressure granulites in the Sudetes, SW Poland. Lithos 95:363–380. doi:10.1016/j.lithos.2006.09.001

Anczkiewicz R, Thirlwall M, Alard O, Rogers NW, Clark C (2012) Diffusional homogenization of light REE in garnet from the Day Nui Con Voi Massif in N-Vietnam: Implications for Sm–Nd geochronology and timing of metamorphism in the Red River shear zone. Chem Geol 318–319:16–30. doi:10.1016/j.chemgeo.2012.04.024

Anderson JR, Kelsey DE, Hand M, Collins WJ (2013) Conductively driven, high-thermal gradient metamorphism in the Anmatjira Range, Arunta region, central Australia. J Metamorph Geol 31:1003–1026. doi:10.1111/jmg.12054

Austrheim H, Erambert M, Boundy TM (1996) Garnets recording deep crustal earthquakes. Earth Planet Sci Lett 139:223–238. doi:10.1016/0012-821X(95)00232-2

Ayers JC, Zhang L, Luo Y, Peters TJ (2012) Zircon solubility in alkaline aqueous fluids at upper crustal conditions. Geochim Cosmochim Acta 96:18–28. doi:10.1016/j.gca.2012.08.027

Baxter EF, Scherer EE (2013) Garnet geochronology: timekeeper of tectonometamorphic processes. Elements 9:433–438. doi:10.2113/gselements.9.6.433

Bloch E, Ganguly J (2015) ^{176}Lu–^{176}Hf geochronology of garnet II: numerical simulations of the development of garnet–whole-rock ^{176}Lu–^{176}Hf isochrons and a new method for constraining the thermal history of metamorphic rocks. Contrib Mineral Petrol 169:1–16. doi:10.1007/s00410-015-1115-x

Bloch E, Ganguly J, Hervig R, Cheng W (2015) ^{176}Lu–^{176}Hf geochronology of garnet I: experimental determination of the diffusion kinetics of Lu^{3+} and Hf^{4+} in garnet, closure temperatures and geochronological implications. Contrib Mineral Petrol 169:1–18. doi:10.1007/s00410-015-1109-8

Buick IS, Storkey A, Williams IS (2008) Timing relationships between pegmatite emplacement, metamorphism and deformation during the intra-plate Alice Springs Orogeny, central Australia. J Metamorph Geol 26:915–936. doi:10.1111/j.1525-1314.2008.00794.x

Caddick MJ, Kohn MJ (2013) Garnet: witness to the evolution of destructive plate boundaries. Elements 9:427–432. doi:10.2113/gselements.9.6.427

Caddick MJ, Konopásek J, Thompson AB (2010) Preservation of garnet growth zoning and the duration of prograde metamorphism. J Petrol 51:2327–2347. doi:10.1093/petrology/egq059

Carlson WD (2002) Scales of disequilibrium and rates of equilibration during metamorphism. Am Mineral 87:185–204

Carlson WD (2006) Rates of Fe, Mg, Mn, and Ca diffusion in garnet. Am Mineral 91:1–11. doi:10.2138/am.2006.2043

Carlson WD (2011) Porphyroblast crystallization: linking processes, kinetics, and microstructures. Int Geol Rev 53:406–445. doi:10.1080/00206814.2010.496184

Carlson WD (2012) Rates and mechanism of Y, REE, and Cr diffusion in garnet. Am Mineral 97:1598–1618. doi:10.2138/am.2012.4108

Cartwright I, Buick IS (1999) Meteoric fluid flow within Alice Springs age shear zones, Reynolds Range, central Australia. J Metamorph Geol 17:397–414. doi:10.1046/j.1525-1314.1999.00205.x

Chakraborty S, Ganguly J (1992) Cation diffusion in aluminosilicate garnets: experimental determination in spessartine-almandine diffusion couples, evaluation of effective binary diffusion coefficients, and applications. Contrib Mineral Petrol 111:74–86. doi:10.1007/bf00296579

Cheng H, King RL, Nakamura E, Vervoort JD, Zhou Z (2008) Coupled Lu–Hf and Sm–Nd geochronology constrains garnet growth in ultra-high-pressure eclogites from the Dabie orogen. J Metamorph Geol 26:741–758. doi:10.1111/j.1525-1314.2008.00785.x

Cook NJ, Ciobanu CL, Meria D, Silcock D, Wade B (2013) Arsenopyrite-pyrite association in an Orogenic Gold Ore: tracing mineralization history from textures and trace elements. Econ Geol 108:1273–1283. doi:10.2113/econgeo.108.6.1273

Corrie SL, Kohn MJ (2008) Trace-element distributions in silicates during prograde metamorphic reactions: implications for monazite formation. J Metamorph Geol 26:451–464. doi:10.1111/j.1525-1314.2008.00769.x

Cygan RT, Lasaga AC (1982) Crystal growth and the formation of chemical zoning in garnets. Contrib Mineral Petrol 79:187–200. doi:10.1007/bf01132887

Dirks PHGM, Wilson CJL (1990) The geological evolution of the Reynolds Range, central Australia: evidence for three distinct structural-metamorphic cycles. J Struct Geol 12:651–665. doi:10.1016/0191-8141(90)90080-I

Dirks PHGM, Hand M, Powell R (1991) The P–T–deformation path for a mid-Proterozoic, low-pressure terrane: the Reynolds Range, central Australia. J Metamorph Geol 9:641–661. doi:10.1111/j.1525-1314.1991.tb00553.x

Dragovic B, Baxter EF, Caddick MJ (2015) Pulsed dehydration and garnet growth during subduction revealed by zoned garnet geochronology and thermodynamic modeling, Sifnos, Greece. Earth Planet Sci Lett 413:111–122. doi:10.1016/j.epsl.2014.12.024

Dumond G, Goncalves P, Williams ML, Jercinovic MJ (2015) Monazite as a monitor of melting, garnet growth and feldspar

recrystallization in continental lower crust. J Metamorph Geol 33:735–762. doi:10.1111/jmg.12150

Dutch R, Hand M (2010) Retention of Sm–Nd isotopic ages in garnets subjected to high-grade thermal reworking: implications for diffusion rates of major and rare earth elements and the Sm–Nd closure temperature in garnet. Contrib Mineral Petrol 159:93–112. doi:10.1007/s00410-009-0418-1

Erambert M, Austrheim H (1993) The effect of fluid and deformation on zoning and inclusion patterns in poly-metamorphic garnets. Contrib Mineral Petrol 115:204–214. doi:10.1007/bf00321220

Florence FP, Spear FS (1991) Effects of diffusional modification of garnet growth zoning on P–T path calculations. Contrib Mineral Petrol 107:487–500. doi:10.1007/bf00310683

Ganguly J (2010) Cation diffusion kinetics in aluminosilicate garnets and geological applications. Rev Mineral Geochem 72:559–601. doi:10.2138/rmg.2010.72.12

George L, Cook NJ, Ciobanu CL, Wade BP (2015) Trace and minor elements in galena: A reconnaissance LA-ICP-MS study. Am Mineral 100:548–569. doi:10.2138/am-2015-4862

Günther D, Frischknecht R, Heinrich CA, Kahlert H-J (1997) Capabilities of an Argon Fluoride 193 nm Excimer Laser for Laser Ablation Inductively Coupled Plasma Mass Spectrometry Microanalysis of Geological Materials. J Anal At Spectrom 12:939–944. doi:10.1039/A701423F

Haines PW, Hand M, Sandiford M (2001) Palaeozoic synorogenic sedimentation in central and northern Australia; a review of distribution and timing with implications for the evolution of intracontinental orogens. Aust J Earth Sci 48:911–928. doi:10.1046/j.1440-0952.2001.00909.x

Hames WE, Menard T (1993) Fluid-assisted modification of garnet composition along rims, cracks, and mineral inclusion boundaries in samples of amphibolite facies schists. Am Mineral 78:338–344

Hand M, Buick IS (2001) Tectonic evolution of the Reynolds-Anmatjira Ranges: a case study in terrain reworking from the Arunta Inlier, central Australia, vol 184. Geological Society, Special Publications, London, pp 237–260. doi:10.1144/gsl.sp.2001.184.01.12

Harlov DE, Wirth R, Hetherington CJ (2011) Fluid-mediated partial alteration in monazite: the role of coupled dissolution–reprecipitation in element redistribution and mass transfer. Contrib Mineral Petrol 162(2):329–348. doi:10.1007/s00410-010-0599-7

Harris C, Vogeli J (2010) Oxygen isotope composition of garnet in the Peninsula Granite, Cape Granite Suite, South Africa: constraints on melting and emplacement mechanisms. S Afr J Geol 113:401–412. doi:10.2113/gssajg.113.4.401

Harris C, Smith HS, le Roex AP (2000) Oxygen isotope composition of phenocrysts from Tristan da Cunha and Gough Island lavas: variation with fractional crystallization and evidence for assimilation. Contrib Mineral Petrol 138:164–175. doi:10.1007/s004100050015

Heinrich CA, Pettke T, Halter WE, Aigner-Torres M, Audétat A, Günther D, Hattendorf B, Bleiner D, Guillong M, Horn I (2003) Quantitative multi-element analysis of minerals, fluid and melt inclusions by laser-ablation inductively-coupled-plasma mass-spectrometry. Geochim Cosmochim Acta 67:3473–3497. doi:10.1016/S0016-7037(03)00084-X

Hellstrom J, Paton C, Woodhead J, Hergt J (2008) Iolite: software for spatially resolved LA-(quad and MC) ICPMS analysis. Miner Assoc Can Short Course Ser 40:343–348

Hetherington CJ, Harlov DE, Budzyń B (2010) Experimental metasomatism of monazite and xenotime: mineral stability, REE mobility and fluid composition. Mineral Petrol 99(3):165–184. doi:10.1007/s00710-010-0110-1

Hickmott D, Spear FS (1992) Major-and trace-element zoning in garnets from calcareous pelites in the NW Shelburne Falls Quadrangle, Massachusetts: garnet growth histories in retrograded rocks. J Petrol 33(5):965–1005. doi:10.1093/petrology/33.5.965

Hollister LS (1966) Garnet Zoning: An Interpretation Based on the Rayleigh Fractionation Model. Science 154:3757. doi:10.1126/science.154.3757.1647

Howell D, Griffin WL, Pearson NJ, Powell W, Wieland P, O'Reilly SY (2013) Trace element partitioning in mixed-habit diamonds. Chem Geol 355:134–143. doi:10.1016/j.chemgeo.2013.07.013

Howlett D, Raimondo T, Hand M (2015) Evidence for 1808–1770 Ma bimodal magmatism, sedimentation, high-temperature deformation and metamorphism in the Aileron Province, central Australia. Aust J Earth Sci 62:831–852. doi:10.1080/08120099.2015.1108364

Huston DL, Maas R, Cross A, Hussey KJ, Mernagh TP, Fraser G, Champion DC (2016) The Nolans Bore rare-earth element-phosphorus-uranium mineral system: geology, origin and post-depositional modifications. Mineral Depos 51:797–822. doi:10.1007/s00126-015-0631-y

Ingham ES, Cook NJ, Cliff J, Ciobanu CL, Huddleston A (2014) A combined chemical, isotopic and microstructural study of pyrite from roll-front uranium deposits, Lake Eyre Basin, South Australia. Geochim Cosmochim Acta 125:440–465. doi:10.1016/j.gca.2013.10.017

Ismail R, Ciobanu CL, Cook NJ, Teale GS, Giles D, Mumm AS, Wade B (2014) Rare earths and other trace elements in minerals from skarn assemblages, Hillside iron oxide–copper–gold deposit, Yorke Peninsula, South Australia. Lithos 184–187:456–477. doi:10.1016/j.lithos.2013.07.023

Jackson SE, Longerich HP, Dunning GR, Freyer BJ (1992) The application of laser-ablation microprobe; inductively coupled plasma-mass spectrometry (LAM-ICP-MS) to in situ trace-element determinations in minerals. Can Mineral 30:1049–1064

Jochum KP, Weis U, Stoll B, Kuzmin D, Yang Q, Raczek I, Jacob DE, Stracke A, Birbaum K, Frick DA, Günther D, Enzweiler J (2011) Determination of Reference Values for NIST SRM 610–617 Glasses Following ISO Guidelines. Geostand Geoanalytical Res 35:397–429. doi:10.1111/j.1751-908X.2011.00120.x

Kelly ED, Carlson WD, Connelly JN (2011) Implications of garnet resorption for the Lu–Hf garnet geochronometer: an example from the contact aureole of the Makhavinekh Lake Pluton, Labrador. J Metamorph Geol 29:901–916. doi:10.1111/j.1525-1314.2011.00946.x

Kelsey DE, Powell R (2011) Progress in linking accessory mineral growth and breakdown to major mineral evolution in metamorphic rocks: a thermodynamic approach in the $Na_2O-CaO-K_2O-FeO-MgO-Al_2O_3-SiO_2-H_2O-TiO_2-ZrO_2$ system. J Metamorph Geol 29:151–166. doi:10.1111/j.1525-1314.2010.00910.x

Kohn MJ (2003) Geochemical zoning in metamorphic minerals. In: Heinrich DH, Karl KT (eds) Treatise on Geochemistry. Pergamon, Oxford, pp 229–261

Kohn MJ (2009) Models of garnet differential geochronology. Geochim Cosmochim Acta 73:170–182. doi:10.1016/j.gca.2008.10.004

Konrad-Schmolke M, Handy MR, Babist J, O'Brien PJ (2005) Thermodynamic modelling of diffusion-controlled garnet growth. Contrib Mineral Petrol 149:181–195. doi:10.1007/s00410-004-0643-6

Konrad-Schmolke M, O'Brien PJ, Heidelbach F (2007) Compositional re-equilibration of garnet: the importance of sub-grain boundaries. Eur J Mineral 19:431–438. doi:10.1127/0935-1221/2007/0019-1749

Konrad-Schmolke M, Zack T, O'Brien PJ, Jacob DE (2008) Combined thermodynamic and rare earth element modelling of garnet growth during subduction: examples from

ultrahigh-pressure eclogite of the Western Gneiss Region, Norway. Earth Planet Sci Lett 272:488–498. doi:10.1016/j.epsl.2008.05.018

Kontonikas-Charos A, Ciobanu CL, Cook NJ (2014) Albitization and redistribution of REE and Y in IOCG systems: Insights from Moonta-Wallaroo, Yorke Peninsula, South Australia. Lithos 208–209:178–201. doi:10.1016/j.lithos.2014.09.001

Lanari P, Riel N, Guillot S, Vidal O, Schwartz S, Pêcher A, Hattori KH (2013) Deciphering high-pressure metamorphism in collisional context using microprobe mapping methods: Application to the Stak eclogitic massif (northwest Himalaya). Geology 41:111–114. doi:10.1130/g33523.1

Lanari P, Vidal O, De Andrade V, Dubacq B, Lewin E, Grosch EG, Schwartz S (2014) XMapTools: A MATLAB©-based program for electron microprobe X-ray image processing and geothermobarometry. Comput Geosci 62:227–240. doi:10.1016/j.cageo.2013.08.010

Lanzirotti A (1995) Yttrium zoning in metamorphic garnets. Geochim Cosmochim Acta 59:4105–4110. doi:10.1016/0016-7037(95)00320-Y

Lapen TJ, Johnson CM, Baumgartner LP, Mahlen NJ, Beard BL, Amato JM (2003) Burial rates during prograde metamorphism of an ultra-high-pressure terrane: an example from Lago di Cignana, western Alps, Italy. Earth Planet Sci Lett 215:57–72. doi:10.1016/S0012-821X(03)00455-2

Lockington JA, Cook NJ, Ciobanu CL (2014) Trace and minor elements in sphalerite from metamorphosed sulphide deposits. Mineral Petrol 108:873–890. doi:10.1007/s00710-014-0346-2

Loomis TP, Nimick FB (1982) Equilibrium in Mn-Fe-Mg aluminous pelitic compositions and the equilibrium growth of garnet. Can Mineral 20:393–410

McLaren S, Sandiford M, Dunlap WJ, Scrimgeour I, Close D, Edgoose C (2009) Distribution of Palaeozoic reworking in the Western Arunta Region and northwestern Amadeus Basin from $^{40}Ar/^{39}Ar$ thermochronology: implications for the evolution of intracratonic basins. Basin Res 21:315–334. doi:10.1111/j.1365-2117.2008.00385.x

Mészáros M, Hofmann BA, Lanari P, Korotev RL, Gnos E, Greber ND, Leya I, Greenwood RC, Jull AJT, Al-Wagdani K, Mahjoub A, Al-Solami AA, Habibullah SN (2016) Petrology and geochemistry of feldspathic impact-melt breccia Abar al' Uj 012, the first lunar meteorite from Saudi Arabia. Meteoritics & Planetary. Science. doi:10.1111/maps.12693

Moore SJ, Carlson WD, Hesse MA (2013) Origins of yttrium and rare earth element distributions in metamorphic garnet. J Metamorph Geol 31:663–689. doi:10.1111/jmg.12039

Morrissey LJ, Hand M, Raimondo T, Kelsey DE (2014) Long-lived high-T, low-P granulite facies metamorphism in the Arunta Region, central Australia. J Metamorph Geol 32:25–47. doi:10.1111/jmg.12056

Norman MD, Pearson NJ, Sharma A, Griffin WL (1996) Quantitative analysis of trace elements in geological materials by Laser Ablation ICPMS: Instrumental operating conditions and calibration values of NIST glasses. Geostand Newsl 20:247–261. doi:10.1111/j.1751-908X.1996.tb00186.x

Otamendi JE, de la Rosa JD, Douce AEP, Castro A (2002) Rayleigh fractionation of heavy rare earths and yttrium during metamorphic garnet growth. Geology 30:159–162. doi:10.1130/0091-7613(2002)030<0159:rfohre>2.0.co;2

Paton C, Hellstrom J, Paul B, Woodhead J, Hergt J (2011) Iolite: Freeware for the visualisation and processing of mass spectrometric data. J Anal At Spectrom 26:2508–2518. doi:10.1039/C1JA10172B

Paul B, Paton C, Norris A, Woodhead J, Hellstrom J, Hergt J, Greig A (2012) CellSpace: A module for creating spatially registered laser ablation images within the Iolite freeware environment. J Anal At Spectrom 27:700–706. doi:10.1039/C2JA10383D

Paul B, Woodhead JD, Paton C, Hergt JM, Hellstrom J, Norris CA (2014) Towards a method for quantitative LA-ICP-MS imaging of multi-phase assemblages: mineral identification and analysis correction procedures. Geostand Geoanalytical Res 38:253–263. doi:10.1111/j.1751-908X.2014.00270.x

Pearce NJG, Perkins WT, Westgate JA, Gorton MP, Jackson SE, Neal CR, Chenery SP (1997) A compilation of new and published major and trace element data for NIST SRM 610 and NIST SRM 612 glass reference materials. Geostand Newsl J Geostand Geoanalysis 21:115–144. doi:10.1111/j.1751-908X.1997.tb00538.x

Petrelli M, Morgavi D, Vetere F, Perugini D (2016) Elemental imaging and petro-volcanological applications of an improved Laser Ablation Inductively Coupled Quadrupole Plasma Mass Spectrometry. Period di Mineral 85:25–39. doi:10.2451/2015PM0465

Pollington AD, Baxter EF (2011) High precision microsampling and preparation of zoned garnet porphyroblasts for Sm–Nd geochronology. Chem Geol 281:270–282. doi:10.1016/j.chemgeo.2010.12.014

Putnis A (2009) Mineral Replacement Reactions. Rev Mineral Geochem 70:87–124. doi:10.2138/rmg.2009.70.3

Putnis A, Austrheim H (2010) Fluid-induced processes: metasomatism and metamorphism. Geofluids 10:254–269. doi:10.1111/j.1468-8123.2010.00285.x

Pyle JM, Spear FS (2003) Yttrium zoning in garnet: Coupling of major and accessory phases during metamorphic reactions. Am Mineral 88:708

Raimondo T, Clark C, Hand M, Faure K (2011) Assessing the geochemical and tectonic impacts of fluid–rock interaction in mid-crustal shear zones: a case study from the intracontinental Alice Springs Orogen, central Australia. J Metamorph Geol 29:821–850. doi:10.1111/j.1525-1314.2011.00944.x

Raimondo T, Clark C, Hand M, Cliff J, Harris C (2012) High-resolution geochemical record of fluid–rock interaction in a mid-crustal shear zone: a comparative study of major element and oxygen isotope transport in garnet. J Metamorph Geol 30:255–280. doi:10.1111/j.1525-1314.2011.00966.x

Raimondo T, Clark C, Hand M, Cliff J, Anczkiewicz R (2013) A simple mechanism for mid-crustal shear zones to record surface-derived fluid signatures. Geology 41(6):711–714. doi:10.1130/g34043.1

Raimondo T, Hand M, Collins WJ (2014) Compressional intracontinental orogens: ancient and modern perspectives. Earth Sci Rev 130:128–153. doi:10.1016/j.earscirev.2013.11.009

Rittner M, Müller W (2012) 2D mapping of LA-ICPMS trace element distributions using R. Comput Geosci 42:152–161. doi:10.1016/j.cageo.2011.07.016

Rubatto D, Williams IS, Buick IS (2001) Zircon and monazite response to prograde metamorphism in the Reynolds Range, central Australia. Contrib Mineral Petrol 140:458–468. doi:10.1007/PL00007673

Rubatto D, Müntener O, Barnhoorn A, Gregory C (2008) Dissolution-reprecipitation of zircon at low-temperature, high-pressure conditions (Lanzo Massif, Italy). Am Mineral 93:1519–1529. doi:10.2138/am.2008.2874

Scherer EE, Cameron KL, Blichert-Toft J (2000) Lu–Hf garnet geochronology: closure temperature relative to the Sm–Nd system and the effects of trace mineral inclusions. Geochim Cosmochim Acta 64:3413–3432. doi:10.1016/S0016-7037(00)00440-3

Schmidt A, Pourteau A, Candan O, Oberhänsli R (2015) Lu–Hf geochronology on cm-sized garnets using microsampling: New constraints on garnet growth rates and duration of

metamorphism during continental collision (Menderes Massif, Turkey). Earth Planet Sci Lett 432:24–35. doi:10.1016/j.epsl.2015.09.015

Schoneveld L, Spandler C, Hussey K (2015) Genesis of the central zone of the Nolans Bore rare earth element deposit, Northern Territory, Australia. Contrib Mineral Petrol 170:1–22. doi:10.1007/s00410-015-1168-x

Sharrad KA, McKinnon-Matthews J, Cook NJ, Ciobanu CL, Hand M (2014) The Basil Cu–Co deposit, Eastern Arunta Region, Northern Territory, Australia: A metamorphosed volcanic-hosted massive sulphide deposit. Ore Geol Rev 56:141–158. doi:10.1016/j.oregeorev.2013.08.008

Skora S, Baumgartner L, Mahlen N, Johnson C, Pilet S, Hellebrand E (2006) Diffusion-limited REE uptake by eclogite garnets and its consequences for Lu–Hf and Sm–Nd geochronology. Contrib Mineral Petrol 152:703–720. doi:10.1007/s00410-006-0128-x

Smit MA, Scherer EE, Mezger K (2013) Lu–Hf and Sm–Nd garnet geochronology: Chronometric closure and implications for dating petrological processes. Earth Planet Sci Lett 381:222–233. doi:10.1016/j.epsl.2013.08.046

Spear FS, Daniel CG (2001) Diffusion control of garnet growth, Harpswell Neck, Maine, USA. J Metamorph Geol 19:179–195. doi:10.1046/j.0263-4929.2000.00306.x

Spear FS, Selverstone J (1983) Quantitative *P–T* paths from zoned minerals: theory and tectonic applications. Contrib Mineral Petrol 83:348–357. doi:10.1007/bf00371203

Taylor SR, McClennan SM (1985) The continental crustal: its composition and evolution. Blackwell, Oxford, p 312

Terry MP, Heidelbach F (2006) Deformation-enhanced metamorphic reactions and the rheology of high-pressure shear zones, Western Gneiss Region, Norway. J Metamorph Geol 24:3–18. doi:10.1111/j.1525-1314.2005.00618.x

Thöni M (2002) Sm–Nd isotope systematics in garnet from different lithologies (Eastern Alps): age results, and an evaluation of potential problems for garnet Sm–Nd chronometry. Chem Geol 185:255–281. doi:10.1016/s0009-2541(01)00410-7

Tirone M, Ganguly J, Dohmen R, Langenhorst F, Hervig R, Becker H-W (2005) Rare earth diffusion kinetics in garnet: Experimental studies and applications. Geochim Cosmochim Acta 69:2385–2398. doi:10.1016/j.gca.2004.09.025

Ubide T, McKenna CA, Chew DM, Kamber BS (2015) High-resolution LA-ICP-MS trace element mapping of igneous minerals: In search of magma histories. Chem Geol 409:157–168. doi:10.1016/j.chemgeo.2015.05.020

Ulrich T, Kamber BS, Jugo PJ, Tinkham DK (2009) Imaging element-distribution patterns in minerals by Laser Ablation–Inductively Coupled Plasma–Mass Spectrometry (LA–ICP–MS). Can Mineral 47:1001–1012. doi:10.3749/canmin.47.5.1001

Vry J, Compston W, Cartwright I (1996) SHRIMP II dating of zircons and monazites: reassessing the timing of high-grade metamorphism and fluid flow in the Reynolds Range, northern Arunta Block, Australia. J Metamorph Geol 14:335–350. doi:10.1111/j.1525-1314.1996.00335.x

Whitney DL (1996) Garnets as open systems during regional metamorphism. Geology 24:147–150. doi:10.1130/0091-7613(1996)024<0147:gaosdr>2.3.co;2

Whitney DL, Broz M, Cook RF (2007) Hardness, toughness, and modulus of some common metamorphic minerals. Am Mineral 92:281–288. doi:10.2138/am.2007.2212

Wilke M, Schmidt C, Dubrail J, Appel K, Borchert M, Kvashnina K, Manning CE (2012) Zircon solubility and zirconium complexation in $H_2O + Na_2O + SiO_2 \pm Al_2O_3$ fluids at high pressure and temperature. Earth Planet Sci Lett 349–350:15–25. doi:10.1016/j.epsl.2012.06.054

Williams IS, Buick IS, Cartwright I (1996) An extended episode of early Mesoproterozoic metamorphic fluid flow in the Reynolds Range, central Australia. J Metamorph Geol 14:29–47. doi:10.1111/j.1525-1314.1996.00029.x

Woodhead JD, Hellstrom J, Hergt JM, Greig A, Maas R (2007) Isotopic and elemental imaging of geological materials by Laser Ablation Inductively Coupled Plasma-Mass Spectrometry. Geostand Geoanalytical Res 31:331–343. doi:10.1111/j.1751-908X.2007.00104.x

Xu J, Ciobanu CL, Cook NJ, Zheng Y, Sun X, Wade BP (2016) Skarn formation and trace elements in garnet and associated minerals from Zhibula copper deposit, Gangdese Belt, southern Tibet. Lithos 262:213–231. doi:10.1016/j.lithos.2016.07.010

Yang P, Pattison D (2006) Genesis of monazite and Y zoning in garnet from the Black Hills, South Dakota. Lithos 88:233–253. doi:10.1016/j.lithos.2005.08.012

Yang P, Rivers T (2001) Chromium and manganese zoning in pelitic garnet and kyanite: Spiral, overprint, and oscillatory (?) zoning patterns and the role of growth rate. J Metamorph Geol 19:455–474. doi:10.1046/j.0263-4929.2001.00323.x

Zhang J, Green HW (2007) Experimental investigation of eclogite rheology and its fabrics at high temperature and pressure. J Metamorph Geol 25:97–115. doi:10.1111/j.1525-1314.2006.00684.x

Zhou B, Hensen BJ (1995) Inherited Sm–Nd isotope components preserved in monazite inclusions within garnets in leucogneiss from East Antarctica and implications for closure temperature studies. Chem Geol 121:317–326. doi:10.1016/0009-2541(94)00130-Z